

## Subgrid surface connectivity for storm surge modeling

Amirhosein Begmohammadi<sup>a,\*</sup>, Damrongsak Wirasat<sup>a</sup>, Zachariah Silver<sup>a,c</sup>, Diogo Bolster<sup>a</sup>, Andrew B. Kennedy<sup>a</sup>, J.C. Dietrich<sup>b</sup>

<sup>a</sup> Environmental Fluid Dynamics, Department of Civil and Environmental Engineering and Earth Sciences, University of Notre Dame, IN, 46556, USA

<sup>b</sup> Department of Civil, Construction, and Environmental Engineering, North Carolina State University, NC, 27695, USA

<sup>c</sup> Department of Physics, Astronomy and Meteorology, Western Connecticut State University, CT, 06810, USA

### ARTICLE INFO

#### Keywords:

Subgrid model  
Storm surge  
Surface connectivity  
Numerical method  
Mathematical modelling

### ABSTRACT

Subgrid modeling to account for unresolved topography within the context of shallow water equations relies on the use of coarse grids for computational efficiency. However, excessively coarse grids can lead to artificial cross flows between hydrologically disconnected areas separated by physical barriers smaller than the grid size. An approach based on introducing cell and edge clones, consisting of connected groups of pixels in each cell, is able to systematically remove such artificial cross flows. Such an approach considers that the subgrid barriers permanently divide flow among clones and effectively restrict flow to a predetermined path. In this work, a simple algorithm, along with the use of an overtopping formula, is proposed to extend the clone approach to a scenario in which clones are allowed to be further split and merged as needed, depending on the surface elevation during a given runtime. The algorithm is intended for accommodating the possibility of the subgrid barriers being inundated and no-longer dividing the flow during an extreme event. The performance of the proposed algorithm is demonstrated through a series of idealized and more realistic test cases, showing considerable improvements over existing methodologies.

### 1. Introduction

Accurate and efficient storm surge prediction is indispensable to prevent destruction of life and property along coastlines. Storm surge modeling is typically based on numerical solution of the depth-averaged Shallow Water Equations (SWE). Broadly speaking, two different strategic approaches have been adopted in modern storm surge models based on their intended purposes. The first is a relatively low resolution ensemble forecast, which relies on using a potentially large ensemble of model runs on relatively coarse computational grids. The benefit of such an approach is that predictions of storm surge before a tropical cyclone makes landfall (Zachry et al., 2015) can be conducted quickly, accounting for uncertainty in a storm's track and intensity. However, the use of a coarse resolution comes at a cost stemming from model errors caused intrinsically by inadequate grid resolution such as unresolved bathymetry, connectivity and unknown roughness from smaller scales. The second category of modeling approaches is to use high resolution simulations, which aim to explicitly resolve as many scales of interest as possible. Such models can be very accurate (Dietrich et al., 2017; Luettich and Westerink, 2004); however, they come with a high computational cost and require a large number of CPU cores to complete a run in a reasonably timely manner (Hope et al., 2013). This limits their applicability with respect to ensemble forecast applications. Thus choosing between

these two options is a trade-off between computational time and accuracy. High resolution models are more accurate, but come with greater computational cost, while low resolution models are fast to execute, but less accurate (Kerr et al., 2013).

A promising intermediate path to achieve models with both accuracy and low cost is through the use of subgrid models, which have recently become an active area of research in the fields focusing on flow over tidal flats and wetlands, urban flooding, and storm surge applications (Kennedy et al., 2019; Wu et al., 2016; Sanders et al., 2008; Sehili et al., 2014; Stelling, 2012; Wang et al., 2014). Note that while there is a rich history of subgrid methods in different aspects of fluid flow and transport modeling (e.g. turbulent flow, porous media flow, multi-phase flow), different systems are needed for application to coastal models with unresolved topography. To this end, if higher resolution topographic and bathymetric information is available and can be directly resolved in computations, it may be more practical to account for its effect with a subgrid model. Over the last decade, the resolution of available topographic data of many coastal areas (and to lesser extent bathymetric data) has increasingly become far finer than the level of resolution affordable for any large scale storm surge model (Danielson et al., 2018). To best exploit the full potential of this data, it may be useful for models to include subgrid corrections. Conceptually, subgrid models are constructed through coarsened properties, such as water levels and

\* Corresponding author.

E-mail address: [abegmoha@nd.edu](mailto:abegmoha@nd.edu) (A. Begmohammadi).

velocities, combined with integral functions of high resolution ground elevations, friction characteristics and any other information that might be available.

Early subgrid models were proposed by Roig (1989); King (2001) and Defina et al. (1994); Defina (2000), where the idea of an artificial porosity, which is a function of the free surface elevation, was introduced to account for partially wet areas. The porosity function is used in the former in the context of a finite element implementation and the latter in deriving a set of governing equations accounting for partially wet/dry areas. To deal with the lack of high resolution topographical data, Defina (2000) introduced an explicit empirical relationship between porosity and depth, based on the assumption that bottom elevations are distributed according to a given probability density function. Sanders et al. (2008) applied volumetric and areal porosities in an integral form of the shallow water equations and discretized them with a finite-volume framework to study flooding in urban areas. They considered the effect of buildings on the flow using a drag formulation and a binary density function that equals zero when corresponding to a building, and one otherwise. However, this model did not account for building interior inundation and is highly sensitive to the mesh used. Guinot (2017); Guinot et al. (2017) improved this integral porosity model by strategically creating a mesh on the computational domain such that cell edges intersect with a water-blocking structures. Without this, the effects of blocking structures do not explicitly appear in this porosity formulation. While this application appears suitable for urban areas, it is restricted in more natural settings, particularly in areas with strong spatial heterogeneity.

Casulli (2009) proposed a semi-implicit finite volume-finite difference approach on a staggered C-grid with a parameter-free subgrid wetting/drying algorithm that uses the porosity function to ensure the positivity of the water height and to account for partial water volume in partially wet cells. The resulting discrete equations are (mildly) nonlinear due to the nonlinear dependency of the porosity function on the surface elevation in the partially wet cells. The proposed algorithm can be used on relatively coarse grids while it incorporates high resolution bathymetric data at the subgrid level. Casulli and Stelling (2011) and Sehili et al. (2014) apply this approach to study flow in Venice Lagoon and the Elbe river, respectively and report that this approach improves model performance with minimal additional computational cost. Platzek et al. (2016) combined the semi-implicit method of Casulli (2009) with a hierarchical grid approach to resolve small-scale topographical features, with the goal of more accurately accounting for regions with significant local energy losses in which the authors posit that, when such losses occur, the subgrid method may not be adequate and a higher grid resolution is required to improve model performance.

Accurately parameterizing bottom drag effects is another essential aspect in the development of subgrid models that has received attention. In Defina (2000); D'alpaos and Defina (2007), the assumption of a constant friction slope was used to derive a formula for bottom stresses accounting for subgrid bathymetry. Casas et al. (2010) presented a method for subgrid roughness parameterization based on turbulence mixing layer theory. Viero and Valipour (2017) introduced anisotropic bottom roughness for some special cases, where models were able to preserve mesh-independence for relatively simple benchmark cases made up of structures with regular shapes and patterns. Based on Casulli's subgrid formulation, Volp et al. (2013) developed a finite volume subgrid model on the staggered C-grid that employs an analytical subgrid velocity of a simplified canonical flow (a channel flow with a uniform flow and constant friction slope) in subgrid corrections of bottom friction and advection terms. The aforementioned corrections improved model performance when there is a large variability of water depth in a coarse grid.

More recently, Kennedy et al. (2019) developed an upscaled form of the 2D shallow water equations through the use of formal averaging methods. The upscaled system of equations are structurally similar to the standard shallow water equations, but have additional terms re-

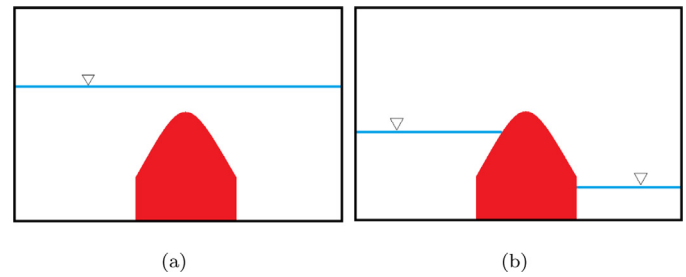


**Fig. 1.** Cross-section of a barrier and water levels of a coarse grid. a) the system can be represented by a single bulk surface elevation and velocity. b) two independent surface elevations and velocities are required to represent the system.

lated to integral properties of the fine-scale topography and flow. They identified different levels of closures of varying complexity. A number of subgrid approaches can be recovered through certain sets of closures. Their model provided a platform to implement subgrid corrections of bottom stresses, advection, and surface gradient terms (the corrections to the gradient of mean water surface elevation are indeed less obvious and are intended for situations where flow characteristics change strongly within an averaging volume).

While the aforementioned advances have led to great improvements, accounting for subgrid connectivity continues to present a substantial challenge due to an assumption of 'subgrid connectedness' for given coarse flow variables. Fig. 1 shows a simple example of subgrid connectedness. When the water surface elevations on either side of a barrier are independent quantities, one water surface elevation is not sufficient to represent the system in the coarse grid. However, if the surface elevation is high enough to inundate the barrier, a single variable may be enough to represent the water surface elevation. Wu et al. (2016), who adopted a pre-storage of necessary quantities to increase computational efficiency, note in their numerical simulation of flow in salt marshes that the level of grid coarsening is limited by bathymetric features, mainly due to the assumptions of a constant surface elevation within a coarse cell; it is suggested that any coarse grid used should be able to resolve general topographical features such as major channels and blocks. Platzek et al. (2016) suggested a hierarchical grid approach utilizing a multigrid concept to resolve small bathymetric features, but this comes with increased computational costs and their approach was intended for quasi-steady state problems. To correct surface connectivity issues, Hodges (2015) developed an automatic edge blocking approach that represents features along Cartesian coarse cell edges; the approach has been used to study many aspects of salt marshes (Li and Hodges, 2019a; 2019b). However, inaccurate approximations of water surface elevation remain unavoidable in coarse grid settings where edge blocking prevents flow within the coarse cell with the block which, depending on the problem at hand, can be detrimental to model predictions.

Recently, Casulli (2019) introduced a cell clone approach to remove an artificial cross flow between disconnected areas within a cell. The approach takes advantage of the nature of the staggered C-grid in that the surface elevation is placed at the cell center and flow velocities that connect two adjacent cells are placed at the edge center. To represent flow paths, each cell and edge are then 'cloned' as many times as necessary based on disjoint groups of connected areas at a given predetermined surface elevation. The surface elevation and velocity among the cell and edge clones of the host cell and host edge are then permitted to have different values, essentially allowing for the possibility of having more degrees of freedom on a single cell and edge. This approach was used to study tidal flow in Sacramento-San Joaquin Delta area, where even relatively coarse grids showed good agreement with high resolution simulations. In this approach, by construction, cell clones of a host cell are permanently disconnected from each other during a simulation. Without modification, the approach does not permit an inundation of subgrid blocking features inside the coarse grid, a scenario likely encountered during extreme events such as storm surge. Casulli (2019) suggests that

this issue can be overcome by using a properly formulated weir formula to re-establish the connection between two adjacent cell clones. While the weir formula permits re-establishment of the connection, it is potentially insufficient when a subgrid barrier is fully submerged. Additionally, the original work of Casulli does not consider a possible scenario in which flow within each clone becomes physically separated by subgrid barriers as the water level recedes (i.e. subgrid connectivity is assumed within the clone). In this study, we propose an extension to Casulli's approach to overcome these limitations.

In §2, we first summarize Casulli's original clone method (Casulli, 2019). Subsequently, we describe a simple approach that is based on further cloning of a cell clone into sub-clones that may or may not be connected depending on the value of the current surface elevation. Sub-clones are allowed to split and merge in order to capture the effect of small barriers that are submerged or emerged when the water surface elevation rises or recedes. In §3, we describe implementation of the proposed approach in the upscaled SWE model of (Kennedy et al., 2019). The performance of the proposed algorithm to deal with flooding and draining is demonstrated in §4, using test problems of increasing complexity and a real setting. Conclusions from the study are drawn in §5.

## 2. Methodology

As standard subgrid approaches assume connectivity throughout a cell, excessive coarsening, while reducing computational cost substantially, can lead to flow connectivity problems, where features that should not be connected in reality are still connected numerically, causing inaccurate estimates of water surface elevation. In section (2.1–2.2), we describe Casulli's method (Casulli, 2019) in which each coarse grid is cloned based on connected pixels to remove artificial cross flows. Building on this, we propose a method that splits a cell clone into sub-clones, where barriers inside a cell clone can emerge at set water surface elevation. In section (2.4), a simple method is presented to connect the sub-clones of a clone.

### 2.1. Computational grid and pixels

Here, we adopt the terminology used in Casulli (2019). More specifically, we consider a raster-based digital elevation model (DEM) with uniform resolution  $\delta$  and parameter  $b$  defined over the entire grid; this might represent the bathymetric depth from still water used to define a computational domain. We denote each single point as a pixel. A grid cell, used as the basis for a computational model, is made up of a group of such pixels. For the highest possible accuracy, a numerical model should account for the information provided by each pixel. Indeed a grid cell can be as small as an individual pixel or as large as the entire computational domain. To maximize efficiency, when using a subgrid model, the computational grid should be allowed to be much coarser than an individual pixel, but still incorporate as much information from each pixel as possible. Let us define the size of grid cell as  $p \times q$  pixels of size  $\delta$ . By partitioning the pixels of a computational domain into  $M \times N$  subarrays representing host cells of size  $\Delta x = p \times \delta$  and  $\Delta y = q \times \delta$ , a coarse grid is obtained. In order to define pixels on a cell edge, the minimum pixel values of two adjacent cells are set as an edge pixel. Thus each pair of two cells has either  $p$  or  $q$  edge pixels. For efficiency, pixels that are not likely to be flooded, i.e. pixels where elevation values are larger than the maximum possible surge are marked as inactive within the computational domain. A cell is marked as inactive if it contains no active pixel. The same is done for cell edges. An active cell edge has at least one active edge pixel, otherwise, the cell edge is marked as inactive.

### 2.2. Cell and edge clones

To begin, we define a reasonable range of surface elevations ( $\eta_{\text{Min}} < \eta < \eta_{\text{Max}}$ ), based on extreme inundation and receding water levels. Pix-

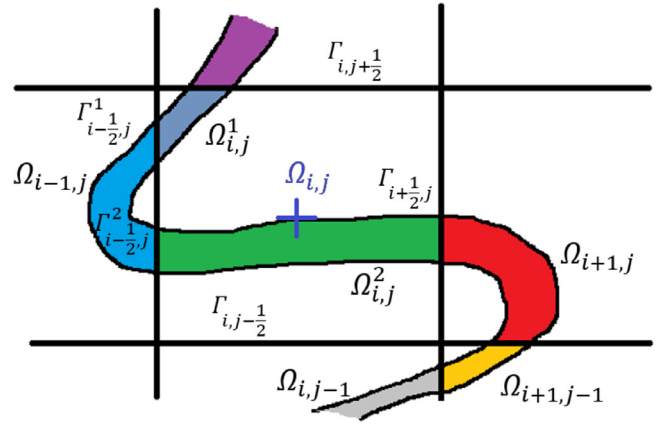
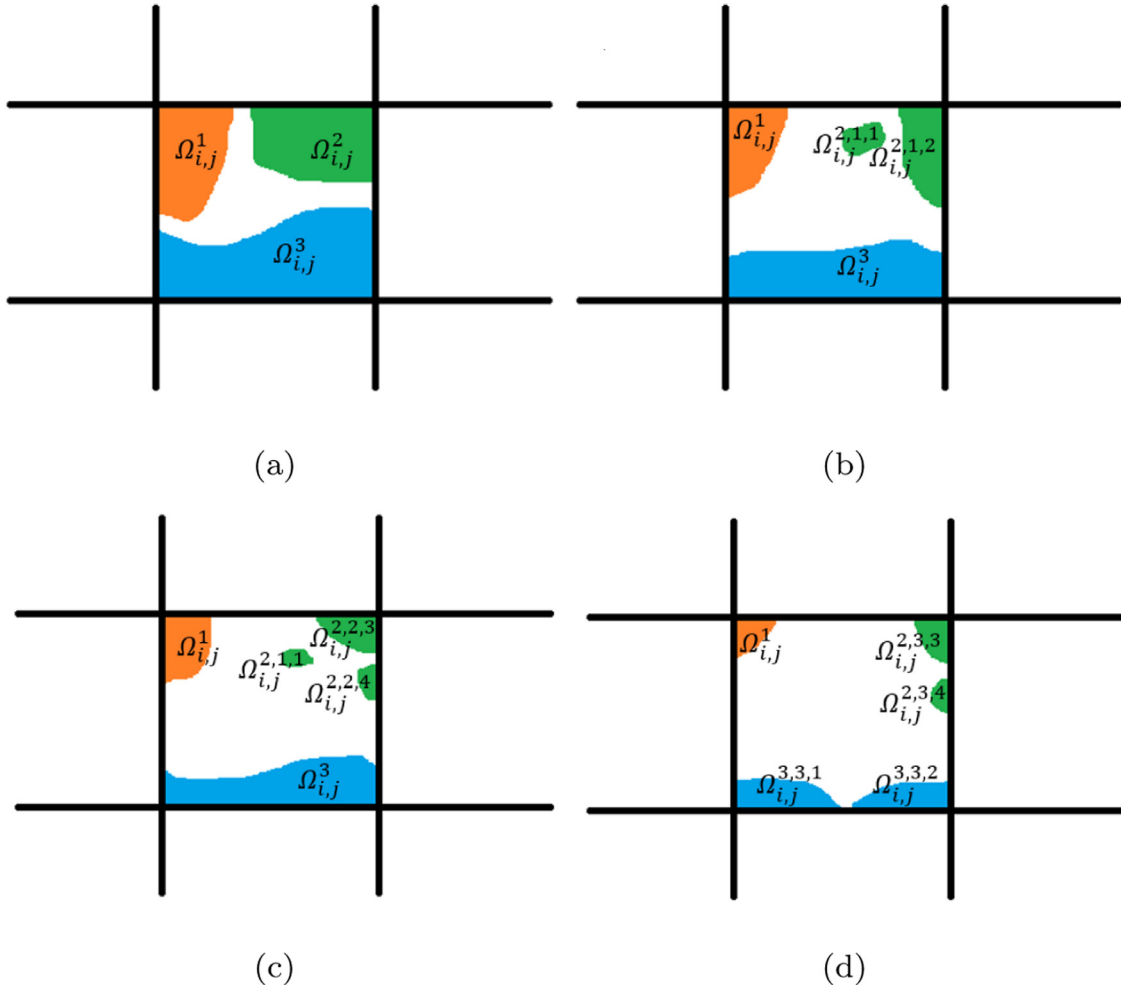


Fig. 2. Host cell, colored area are active pixels, thick gridded black lines show the coarse grid.

els that are not likely to be flooded are marked as inactive ( $-b > \eta_{\text{Max}}$ ). The remaining pixels are called active pixels. If there is a continuous path of active pixels between any two pixels, these two pixels are called connected pixels. Within a grid cell, there may be multiple groups of connected pixels that are separated from one other. Similarly, edge pixels that are not likely to be flooded ( $-b_{\text{edge}} > \eta_{\text{Max}}$ ) are marked as inactive edge pixels. Each cell edge that contains one or more active pixels is an active edge; otherwise it is an inactive edge.

At the maximum surface elevation  $\eta_{\text{Max}}$ , the host cell is cloned a sufficient number of times based on the number of separate groups of connected pixels. Each clone of a host cell only contains one group of connected pixels. The clones of a host cell are assumed not connected with each other under any extreme situation (to fully achieve this condition,  $\eta_{\text{Max}}$  should be sufficiently high; in practice, a reasonable value of  $\eta_{\text{Max}}$  is the maximum probable surge height for the area of interest based on the historical surge event). Each clone of a host cell has a constant water surface elevation, but this can be different among the clones within the same host cell. Similarly, a host edge pairing two host cells is cloned a sufficient number of times where each edge clone is a group of edge pixels shared by two clones of such neighboring cells. These edge clones provide the connectivity information between each host cell and its neighbours. Each edge clone of a host edge is assumed to have a constant discrete velocity perpendicular to the edge (either  $u$  or  $v$ ) but this velocity can be different among edge clones of the same host edge. Therefore, the cell and edge clone approach provides more degrees of freedom for the host cell that leads to a more accurate representation within the coarse grid, where small scale structures disconnect flow.

To help further illustrate our point, the grid cells, active pixels, and cell and edge clones of a meandering river are shown in Fig. 2. Groups of connected pixels are highlighted with different colors. Let us focus on the host cell  $(i, j)$  located in the center of the domain. It can be seen that there are two disjoint groups of connected pixels  $\Omega_{i,j}^1$  and  $\Omega_{i,j}^2$ . On its western (left) edge  $\Gamma_{i-1/2,j}$ , there are two groups of active edges  $\Gamma_{i-1/2,j}^1$  and  $\Gamma_{i-1/2,j}^2$ ; the former connects the clone  $\Omega_{i,j}^1$  and  $\Omega_{i-1,j}$  and the latter connects  $\Omega_{i,j}^2$  and  $\Omega_{i-1,j}$ ; on its northern (top) edge, the set of active edge pixels  $\Gamma_{i,j+1/2}$  connects  $\Omega_{i,j}^1$  and  $\Omega_{i,j+1}$ ; on its eastern (right) edge,  $\Gamma_{i+1/2,j}$  connects  $\Omega_{i,j}^2$  and  $\Omega_{i+1,j}$ ; there is an inactive edge in the south (bottom) edge ( $\Gamma_{i,j-1/2}$ ). So this host cell has two cell clones, which could have different water surface elevations; the host edge to the west (left) of this host cell has two edge clones, which could have different  $u$  velocity; the host edges to east (right) and north (top) have single values of the  $u$  and  $v$  velocity, respectively; the host edge on the south (bottom) is inactive (and thus is treated as a dry edge). It is important to note that cell clones of a host cell share the same geometric center. Edge clones of



**Fig. 3.** Host cell, colored area are active pixels, thick gridded black lines show the coarse grid. a) cell clones at  $\eta = \eta_{Max}$ . b) cell clones and sub-clones at  $\eta_1 < \eta_{Max}$ . c) cell clones and sub-clones at  $\eta_2 < \eta_1$ . d) cell clones and sub-clones at  $\eta = \eta_{Min}$ . Note that  $\Omega^{a,b,c}$  a = cell clone, b - level, c = sub-clone number.

a host cell have the same length and geometric position of an edge cell. Therefore, a cell clone is a copy of the host cell including a connected path of active pixels, and a clone edge is a copy of the active host edge including a connected path between two neighbouring cell clones of two adjacent cells. Furthermore, each active pixel belongs to just one single clone of a host cell and each active pixel of an edge clone belongs to just one edge clone.

### 2.3. Sub-clones

If a cell is cloned sufficiently at the maximum surface elevation to remove artificial cross flows, such cross flow may still exist at surface elevations less than  $\eta_{Max}$ , i.e. in between  $\eta_{Min} < \eta < \eta_{Max}$ , as new barriers appear at lower surface elevations and split a cell clone into two or more groups of connected pixels (as illustrated in Fig. 3). Each of these groups of connected pixels is hereafter called a sub-clone. A sub-clone of a cell clone may or may not be connected to one sub-clone or multiple sub-clones of the host cell clone at a given surface elevation. For simplicity and efficiency purposes, the horizontal size (an area) of a sub-clone is considered as a constant during the simulation. For each sub-clone, a minimum water surface elevation is defined based on the minimum bathymetry of the sub-clone to determine the wet/dry condition of the sub-clone. If the water surface elevation of a sub-clone goes under the minimum bathymetry of the sub-clone, the sub-clone is removed from the computational domain due to the dry condition of the sub-clone.

Fig. 3 shows an example of host cells and their wet areas at four different water levels ( $\eta_{Max} = \eta_0 > \eta_1 > \eta_2 > \eta_3 = \eta_{Min}$ ). At the maximum surface elevation  $\eta_{Max}$ , three cell clones ( $\Omega_{i,j}^1, \Omega_{i,j}^2, \Omega_{i,j}^3$ ) can be seen. These three cell clones are not connected with each other. By reducing the water surface elevation to  $\eta_1$ , cell clone number 2 ( $\Omega_{i,j}^2$ ) is divided into two disconnected sub-clones ( $\Omega_{i,j}^{2,1,1}$  and  $\Omega_{i,j}^{2,1,2}$ ). These two sub-clones are disconnected at the specific surface elevation ( $\eta_n$ ). Hereafter, this surface elevation is called the connectivity surface elevation (a lengthy notation  $\eta_{h,(i,j)}^{n,m}$  where  $n$  denotes a clone number and  $m$  a sub-clone level will be used to precisely indicate the connectivity surface elevation when some ambiguity arise). This water surface elevation is used to connect sub-clone  $\Omega_{i,j}^{2,1,1}$  to sub-clone  $\Omega_{i,j}^{2,2,2}$ . At water surface elevation  $\eta_2$ , this clone is divided into three sub-clones ( $\Omega_{i,j}^{2,1,1}$ ,  $\Omega_{i,j}^{2,2,1}$ , and  $\Omega_{i,j}^{2,2,2}$ ). Note that sub-clone  $\Omega_{i,j}^{2,1,2}$  is divided into two sub-clones at the connectivity surface elevation  $\eta_2 = \eta_{\Omega_{i,j}^2}(\eta_2)$ . The connectivity surface elevation can be found for each sub-clone by sampling reduced water surface elevations. At surface elevation  $\eta_3$ , one of the sub-clones ( $\Omega_{i,j}^{2,1,1}$ ) disappears altogether due to the dry condition. Thus for surface elevations in the range of  $\eta_{Min} < \eta_3$ , sub-clone  $\Omega_{i,j}^{2,1,1}$  should not be considered during computations. Fig. 4 shows the algorithm to find cell clones and sub-clones of a domain step by step.

A sub-clone has four edges. At each edge, a velocity, perpendicular to the edge, is defined. If there are no active pixels on one sub-clone edge, that edge is inactive and it is not connected to the adjacent host

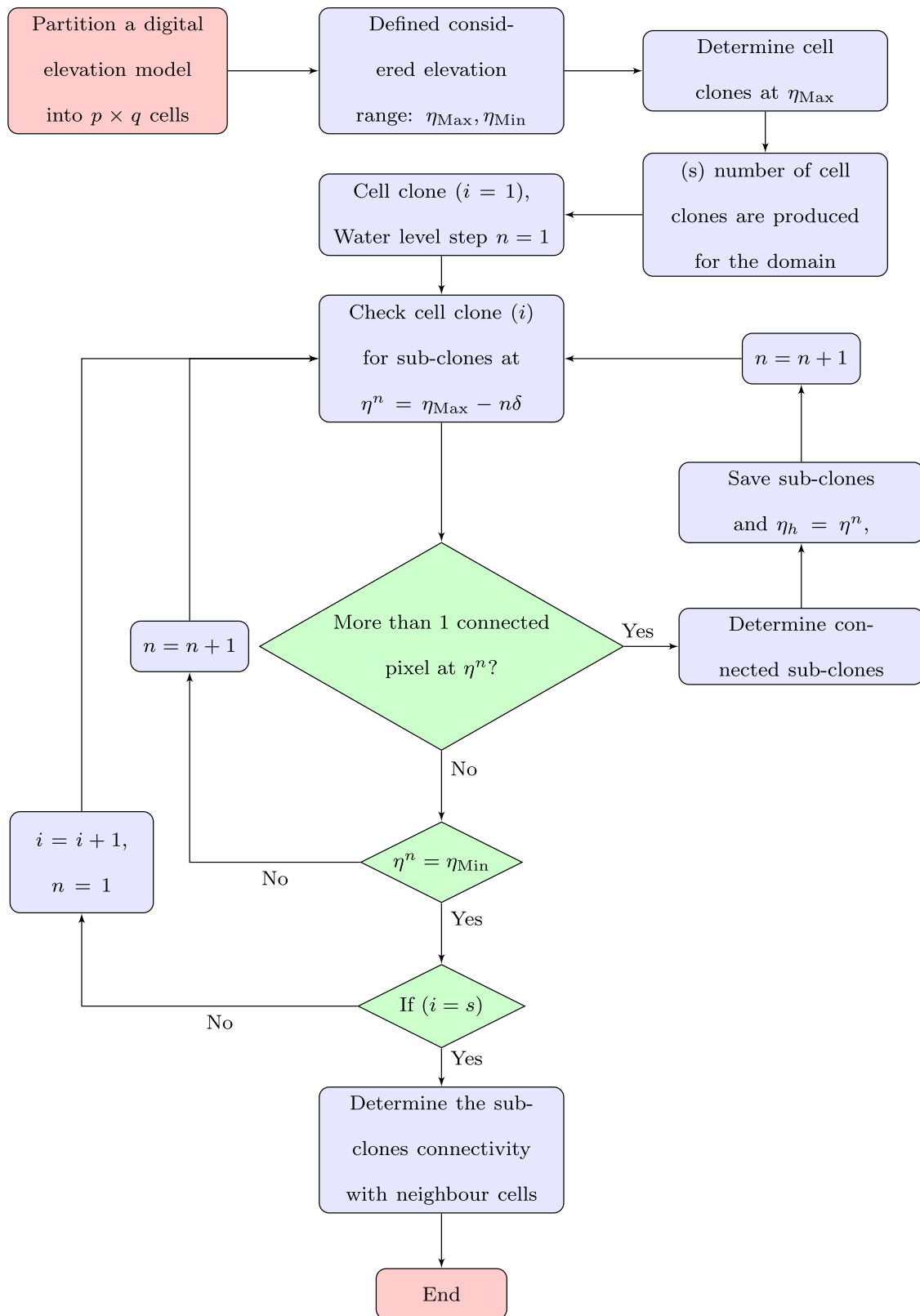


Fig. 4. Flowchart representation of algorithm to find cell clones and sub-clones of a coarse cell. (s) is the number of cell clones.  $\delta = \frac{\eta_{Max} - \eta_{Min}}{r}$ . (r) is the number of cell clone levels.

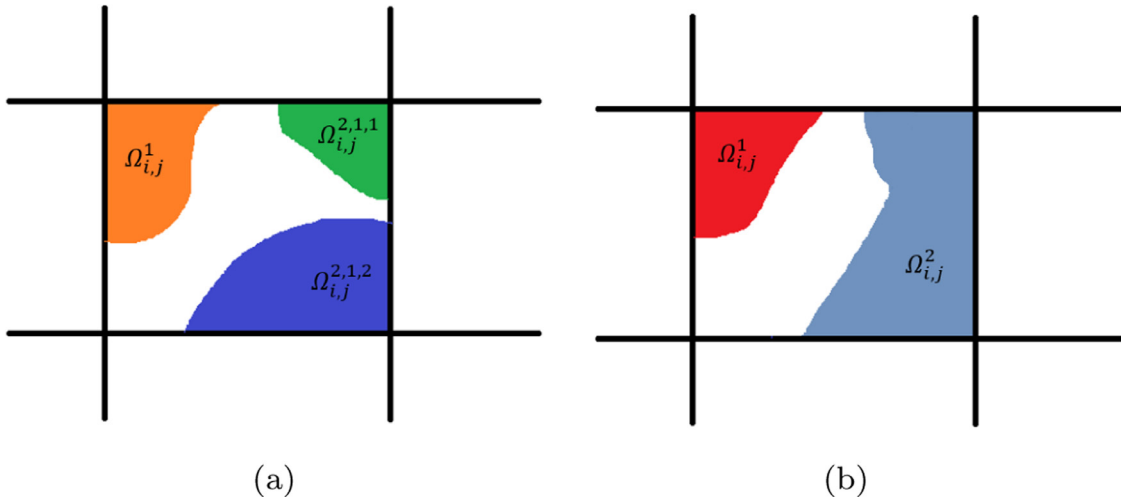


Fig. 5. Host cell- a) the host cell at surface elevation of  $\eta_1$ . b) the host cell at surface elevation of  $\eta_2 > \eta_1$ .

cell. However, it is possible that a sub-clone edge could be active within some range of the water surface elevations and be inactive in the others.

Note that sub-clones of a cell clone share the same size and geometric center as the host cell. Therefore, a sub-clone is a copy of the host cell including a connected path of active pixels. Furthermore, each active pixel of a clone belongs to just one single sub-clone of a cell clone. A sub-clone edge has the same geometric location and length of the host cell and each active pixel of an edge cell belongs to just one sub-clone of a cell clone. To reduce the computational cost, isolated sub-clones that are much smaller than the coarse grid are removed from the computational domain. (If a sub-clone does not connect with the cell clones or sub-clones of the neighbor cells, it is considered an isolated sub-clone)

#### 2.4. Merging and splitting sub-clones

In this section, we propose a method to connect sub-clones of a cell clone when blocking structures inside the cell clone are submerged. Fig. 5a shows the host cell  $\Omega_{i,j}$  at the maximum surface elevation  $\eta_{Max}$ . This cell has three cell clones of  $\Omega_{i,j}^1$ ,  $\Omega_{i,j}^2$  and  $\Omega_{i,j}^3$ . Fig. 5b shows the sub-clones and clones of this host cell at connectivity surface elevation  $\eta_{h,(i,j)}^{2,1}$ . It can be seen that cell clone  $\Omega_{i,j}^2$  splits into two sub-cell clones  $\Omega_{i,j}^{2,1,1}$  and  $\Omega_{i,j}^{2,1,2}$  (as surface elevation increases above the connectivity surface elevation, sub-clones are merged). Therefore sub-clones  $\Omega_{i,j}^{2,1,1}$  and  $\Omega_{i,j}^{2,1,2}$  at surface elevations  $\eta_{h,(i,j)}^{2,1} < \eta$  are submerged and one sub-clone is considered instead. During the simulation, when the water surface elevation reaches the connectivity surface elevation ( $\eta_{h,(i,j)}^{2,1}$ ) for two connected or more connected sub-clones, they are merged and one cell clone is considered ( $\Omega_{i,j}^2$ ). This cell clone has one surface elevation, which is the average surface elevation of the connected sub-clones when the surface elevation of each sub-clone passes the connectivity surface elevation.

However, it is possible that the surface elevation of one of the sub-clones reaches the connectivity surface elevation ahead of the other ones. Here, a sub-clone cell which is connected to the inlet (has the higher water surface elevation) is called a source sub-clone and the other sub-clones are called receiver sub-clones. To deal with this, an overflow formula is used to connect the source sub-clone to the receiver sub-clones until the water surface elevation of the receiver clone reaches the connectivity water surface elevation. Thereafter, one cell clone or sub-clone with one constant surface elevation can be considered.

For simplicity, the overflow is modeled as a sharp-crested weir, although we note that this could readily be changed as needed should a better option be available. A sharp-crested weir is an overflow structure consisting of a vertical plate with a sharp-edged crest mounted perpen-

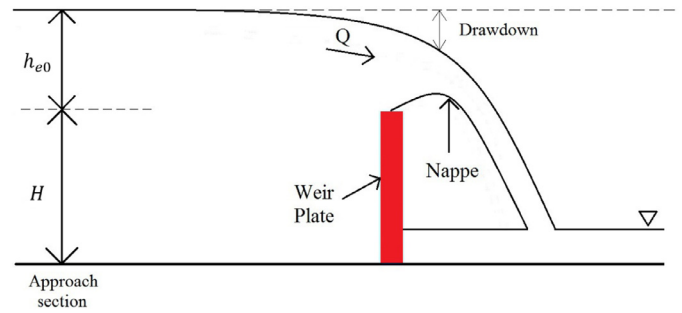


Fig. 6. Sharp-crested weir.

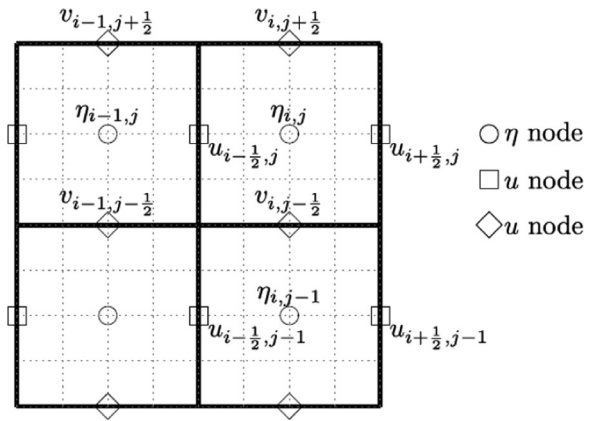


Fig. 7. Staggered grid with locations of the surface elevation and velocity components.

dicular to the flow direction, as shown in Fig. 6. A simple empirical formula is used to assign an overflow between disconnected sub-clones of a cell clone.

Downstream of a sharp-crested weir, free flow occurs when the weir allows free access of air under the nappe. The weir will be submerged if downstream water rises near or above the crest elevation. Based on the experimental work of Kindsvater (Kindsvater and Carter, 1959), the following formula is used to approximate discharge

$$Q = k_w \sqrt{2g} L_{ew} h_{e0}^{(3/2)} \quad (1)$$

where  $k_w = 2/3$  is a constant,  $L_{ew}$  is effective width, and  $h_{e0}$  is effective depth in regard to the shape of weir.

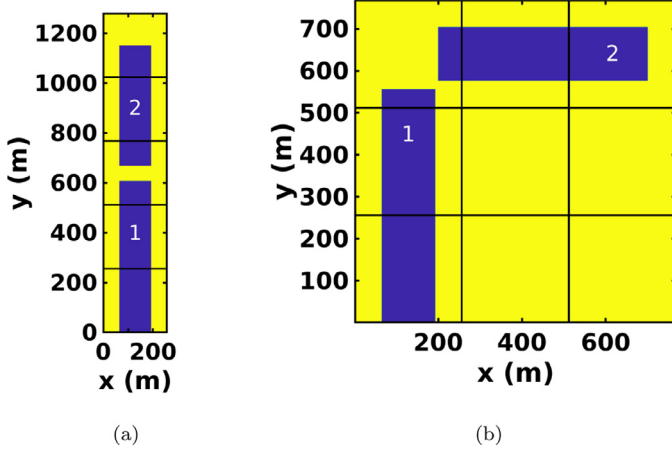


**Fig. 8.** Channel block systems alongside the location of coarse grids. Blue area is wet  $b = -3$  m and yellow area is dry  $b = 25$  m. Solid black lines are the location of coarse grid. The time series of surface elevation are recorded at Station 1,2. a) is channel configuration A. b) is channel configuration B. (For interpretation of the references to colour in this figure legend, the reader is referred to the web version of this article.)

In the context of a cell clone, we can calculate discharge from the source cell to the receiver cell based on (1) for each time step until the water surface elevation of receiver cell reaches the connectivity water surface elevation ( $\eta_h$ ). Once such a state is reached, the average water surface elevation of the source and receiver clone is computed for a single constant water surface elevation of the merged cell clone by means of

$$\eta_{MC} = \frac{V_{MC}}{A_{MC}} - b_{MC}, \quad V_{MC} = V_{SC} + V_{RC} \quad (2)$$

where  $A$  and  $V$  denote the area and volume of a cell,  $b$  is the averaged bathymetric depth where the average is the combination of wet areas of connected cells, and subscripts  $MC$ ,  $SC$ , and  $RC$  denote merged sub-clone, source sub-clone, and receiver sub-clone, respectively. To conserve mass in any situations, a better approach can be employed where the volume of a merged sub-clone is computed from the high resolution bathymetric data as a function of the surface elevation, i.e. given the volume of the merged sub-clone from Eq. (2), the water surface elevation is determined from the inverse relationship of the volume and the water surface elevation curve of the merged cell.

For the parameters in (1), we use  $h_{e0} = \eta_{source} - \eta_h$  and for simplicity  $L_{ew} = \Delta x$  or  $\Delta y$ . At each time step, discharge is calculated for the receiver clone.

### 3. Governing equations

#### 3.1. Subgrid model discretization

The two-dimensional depth-averaged shallow water equations are considered. Conservation of mass is given by

$$\frac{\partial H}{\partial t} + \frac{\partial HU}{\partial x} + \frac{\partial HV}{\partial y} = 0, \quad (3)$$

where  $t$  denotes time and  $U(x, y, t)$  and  $V(x, y, t)$  are the vertically averaged water velocity components in the x-direction and y-direction, respectively. Here,  $H = \eta + b(x, y)$  is the local total water depth, where  $\eta$  denotes the surface elevation and  $b(x, y)$  bathymetric depth. The momentum equations in the conservative form are

$$\begin{aligned} \frac{\partial HU}{\partial t} + \frac{\partial}{\partial x}(HUU) + \frac{\partial}{\partial y}(HUV) + gH \frac{\partial \eta}{\partial x} = & -\frac{\tau_{bx} - \tau_{sx}}{\rho} \\ - \frac{1}{\rho} \frac{\partial P_A}{\partial x} + f_c HV + \frac{1}{\rho} \left( \frac{\partial H \tau_{xx}}{\partial x} + \frac{\partial H \tau_{xy}}{\partial y} \right) \end{aligned} \quad (4)$$

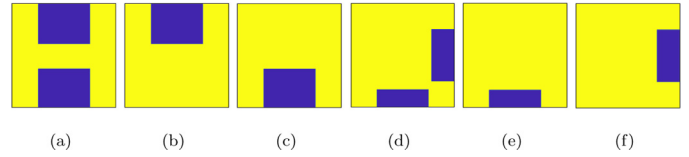


**Fig. 9.** Blocked cells and their clones: a)-c) channel configuration A. a) block cell, b) cell clone 1, c) cell clone 2, d)-f) channel configuration B. d) block cell, e) cell clone 1, f) cell clone 2.

and

$$\begin{aligned} \frac{\partial HV}{\partial t} + \frac{\partial}{\partial x}(HVV) + \frac{\partial}{\partial y}(HVV) + gH \frac{\partial \eta}{\partial y} = & -\frac{\tau_{by} - \tau_{sy}}{\rho} \\ - \frac{1}{\rho} \frac{\partial P_A}{\partial y} + f_c HU + \frac{1}{\rho} \left( \frac{\partial H \tau_{yx}}{\partial x} + \frac{\partial H \tau_{yy}}{\partial y} \right), \end{aligned} \quad (5)$$

where  $\tau_b$  and  $\tau_s$  are bottom stresses and surface stresses, respectively,  $P_A$  is local atmospheric pressure,  $f_c$  is the Coriolis parameter, and  $\tau_{xx}$ ,  $\tau_{xy} = \tau_{yx}$ , and  $\tau_{yy}$  denotes the lateral stresses due to turbulence mixing. For the bottom stresses, we consider quadratic formula:

$$\frac{\tau_b}{\rho} = \gamma U, \quad \gamma = C_f |U| \quad (6)$$

where  $C_f$  is a bottom drag coefficient. For simplicity, in this study, the Coriolis force, wind stress, atmospheric pressure, lateral stresses are neglected, although they can be readily included should they be required.

#### 3.2. Upscaled equations

We consider the upscaled SWEs proposed by Kennedy et al. (2019). These equations are derived from formally applying averaging techniques (Whitaker, 2013) to the SWEs presented in the previous section. The upscaled mass equation is

$$\frac{\partial V_w(\langle \eta \rangle)}{\partial t} + \frac{\partial \langle H \rangle \langle U \rangle}{\partial x} + \frac{\partial \langle H \rangle \langle V \rangle}{\partial y} = 0, \quad (7)$$

where  $V_w(\langle \eta \rangle)$  denotes the wet volume per unit area for a given wet-averaged surface elevation  $\langle \eta \rangle$ ,  $\langle U \rangle = \int HU dV / \int H dV$  is the velocity vector averaged to the grid level, and  $\langle H \rangle$  denotes grid-averaged water depth. The upscaled momentum equations are

$$\begin{aligned} \langle H \rangle \frac{\partial \langle U \rangle}{\partial t} - \langle U \rangle \nabla \cdot (\langle U \rangle \langle H \rangle) + \frac{\partial}{\partial x} (C_{UU} \langle U \rangle \langle V \rangle \langle H \rangle) \\ + \frac{\partial}{\partial y} (C_{UV} \langle U \rangle \langle U \rangle \langle H \rangle) = -g \langle H \rangle \left( C_{\eta,xx} \frac{\partial \langle \eta \rangle}{\partial x} + C_{\eta,xy} \frac{\partial \langle \eta \rangle}{\partial y} \right) \\ - \phi | \langle U \rangle | (C_{M,fx} \langle U \rangle + C_{M,fy} \langle V \rangle) \end{aligned} \quad (8)$$

$$\begin{aligned} \langle H \rangle \frac{\partial \langle V \rangle}{\partial t} - \langle V \rangle \nabla \cdot (\langle U \rangle \langle H \rangle) + \frac{\partial}{\partial x} (C_{VU} \langle V \rangle \langle U \rangle \langle H \rangle) \\ + \frac{\partial}{\partial y} (C_{VV} \langle V \rangle \langle V \rangle \langle H \rangle) = -g \langle H \rangle \left( C_{\eta,yx} \frac{\partial \langle \eta \rangle}{\partial x} + C_{\eta,yy} \frac{\partial \langle \eta \rangle}{\partial y} \right) \\ - \phi | \langle U \rangle | (C_{M,fx} \langle U \rangle + C_{M,fy} \langle V \rangle) \end{aligned} \quad (9)$$

where  $\langle \cdot \rangle$  brackets denote grid averaged quantities, except for velocity and water surface elevation, where they are understood as a volume average and wet (intrinsic) average, respectively. In 8–(9),  $\phi = A_w/A_G$  denotes the wet area fraction;  $C_{UU}$ ,  $C_{UV}$ ,  $C_{VU}$ ,  $C_{VV}$  are coefficients accounting for subgrid corrections associated with the nonlinear convection terms;  $C_\eta$  is the subgrid correction of the surface gradient coefficient; and  $C_M$  is effective bottom stress coefficient.

Several closures for determining the subgrid correction parameters are proposed in Kennedy et al. (2019). Here, we consider the so called Level 0 closure. This closure uses fractional wetting and drying over the grid cell for mass correction, but makes no sophisticated attempt at

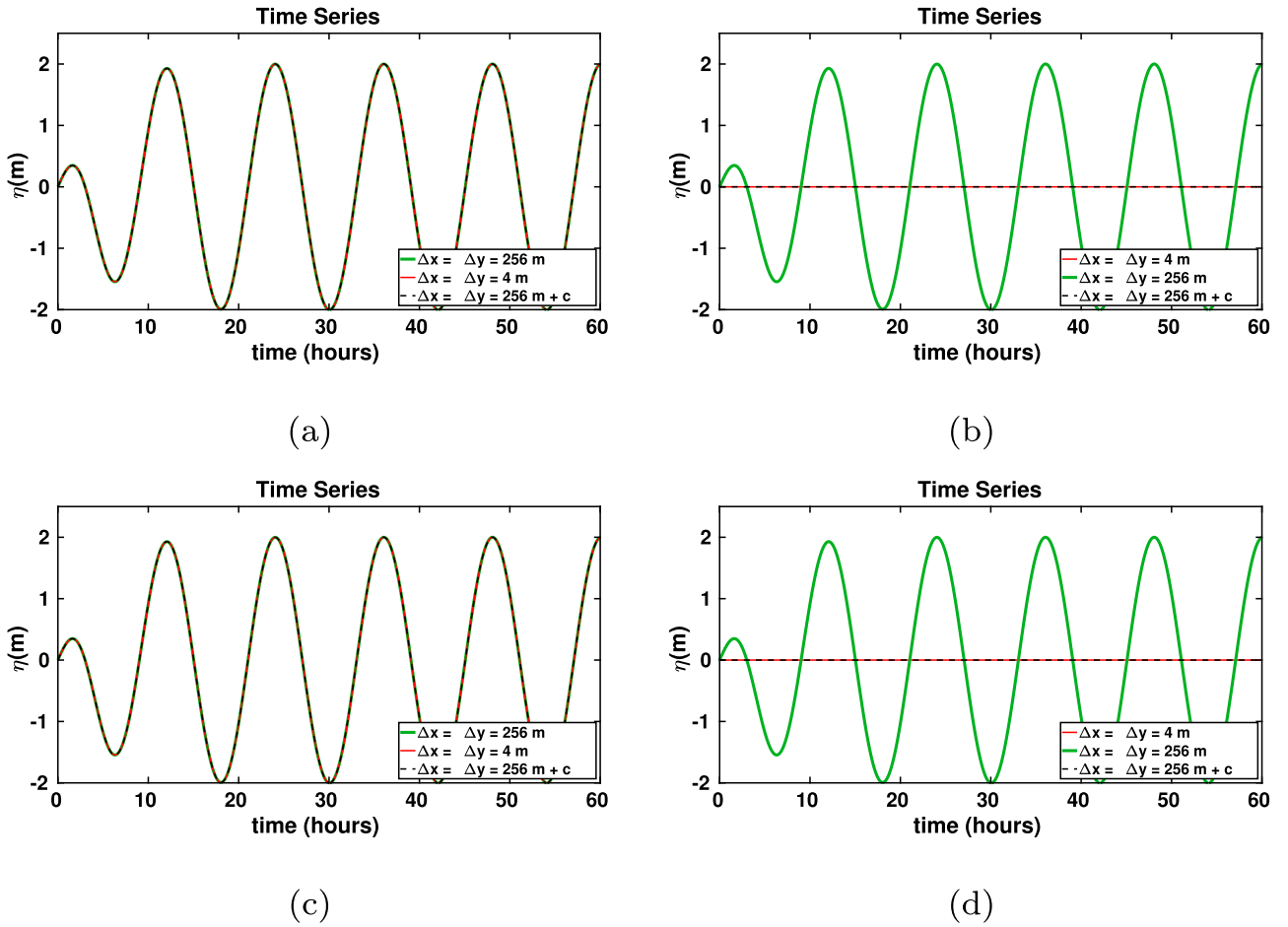


Fig. 10. Time series of surface elevation  $\eta$ . a) channel configuration A. Station 1 (connected to the inlet). b) channel configuration A. Station 2 (in the secondary channel). c) channel configuration B. Station 1 (connected to the inlet). d) channel configuration B. Station 2 (in the secondary channel).

subgrid corrections for the momentum convection and surface gradient terms. More precisely, subgrid parameter are set to:

$$C_{\eta,xx} = C_{\eta,yy} = 1, \quad C_{\eta,xy} = C_{\eta,yx} = 0, \quad (10)$$

$$C_{M,f,xx} = C_{M,f,yy} = \langle C_f \rangle_G, \quad C_{M,f,xy} = C_{M,f,yx} = 0, \quad (11)$$

$$C_{UU} = C_{VV} = C_{UV} = C_{VU} = 1, \quad (12)$$

### 3.3. Discretization

The upscaled three Eqs. (7)–(9) have three unknown solution functions  $\langle \eta \rangle$ ,  $\langle U \rangle$ , and  $\langle V \rangle$  (the averaged water depth  $\langle H \rangle = V_w$  is taken to be a known variable and determined from  $\langle \eta \rangle$  and a given DEM  $b(x, y)$ ). They are discretized on a staggered C-grid with a semi-implicit finite difference method (see Fig. 7). The unknown variable  $\langle \eta \rangle$  is placed at the cell-center and  $\langle U \rangle$ ,  $\langle V \rangle$  are located at the midpoint of the vertical and horizontal cell edges, respectively. The advection term in (8) and (9) is discretized explicitly via an upwind scheme. The surface gradient and bottom stress terms in the momentum equations and velocities in the continuity Eq. (7) are discretized implicitly to avoid restrictions on  $\Delta t$  from the  $\sqrt{gh}$  wave and stiff bottom friction source term when the value  $C_M$  is large. We refer to Kennedy et al. (2019) for more detailed account of the numerical method. Below we describe the modification of the method to include the methodology described in Section 2.

To keep the notation simple,  $\eta$ ,  $H$ ,  $u$ , and  $v$  will be used to refer to the averaged variables  $\langle \eta \rangle$ ,  $\langle H \rangle$ ,  $\langle U \rangle$ , and  $\langle V \rangle$ , respectively. Suppose

that, at the time level  $t = \Delta t$ , we have a set of wet clone edges and cell clones with at least one wet edge. Note that cell clones correspond to sub-clones when the water surface elevation in a clone drops below the connectivity water surface elevation level (see Section 2.4), which determines particular sub-clones to be considered. With such the sets at hand, the discretization of the governing equations is as follows.

A semi-implicit discretization of the momentum equations is written for each ‘clone’ edge, which could be a sub-clone of a host edge. The discretization of the  $x$ - and  $y$ -momentum equations carried out at the vertical and horizontal edges are, respectively:

$$u_{i+\frac{1}{2},j}^{n+1} = \frac{1}{H_{i+\frac{1}{2},j}^*} \left[ H_{i+\frac{1}{2},j}^n u_{i+\frac{1}{2},j}^n - \Delta t F_{i+\frac{1}{2},j}^n - g \frac{\Delta t}{\Delta x} H_{i+\frac{1}{2},j}^n (\eta_{i+1,j}^{n+1} - \eta_{i,j}^{n+1}) \right], \quad (13)$$

and

$$v_{i,j+\frac{1}{2}}^{n+1} = \frac{1}{H_{i,j+\frac{1}{2}}^*} \left[ H_{i,j+\frac{1}{2}}^n v_{i,j+\frac{1}{2}}^n - \Delta t G_{i,j+\frac{1}{2}}^n - g \frac{\Delta t}{\Delta y} H_{i,j+\frac{1}{2}}^n (\eta_{i,j+1}^{n+1} - \eta_{i,j}^{n+1}) \right], \quad (14)$$

where

$$H_{i+\frac{1}{2},j}^* = \frac{1}{H_{i+\frac{1}{2},j}^n + \gamma_{i+\frac{1}{2},j} \Delta t}, \quad H_{i,j+\frac{1}{2}}^* = \frac{1}{H_{i,j+\frac{1}{2}}^n + \gamma_{i,j+\frac{1}{2}} \Delta t},$$

and  $F_{i+\frac{1}{2},j}$  and  $G_{i,j+\frac{1}{2}}$  represent the discretization of the advection terms (see Kennedy et al. (2019) for more detail of these terms). It is emphasized that, in (13)–(14), the notations are overloaded for notational simplicity. More specifically, in (13),  $u_{i+\frac{1}{2},j}$ ,  $H_{i+\frac{1}{2},j}$  must be interpreted as

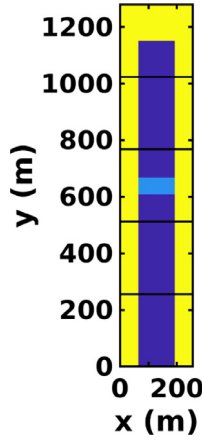


Fig. 11. Channel and block system. Dark blue is wet area ( $b = -3$  m), yellow is dry area ( $b = 25$  m) and light blue is a blockage ( $b = 0$  m). Solid black lines are the location of coarse grids. (For interpretation of the references to colour in this figure legend, the reader is referred to the web version of this article.)

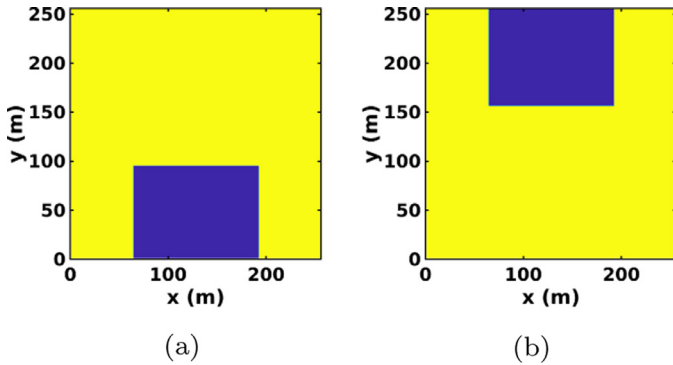


Fig. 12. Sub-clones of the block cell with  $\eta_h = 0$ . a) sub-clone 1. b) sub-clone 2.

the  $u$ -velocity and water depth associated with a (sub-) clone edge of the  $(i, j + \frac{1}{2})$  host edge;  $\eta_{i+1,j}$  and  $\eta_{i,j}$  are the surface elevations of two (sub-)clones from neighboring host cells to which the connected path is through the clone edge considered. The approximate solution variables in (14) are interpreted in an analogous manner.

For each ‘clone’ cell, which could be a sub-clone, of a host cell, the discretization of continuity Eq. (7) with the Euler backward time discretization is considered

$$\frac{V(\eta_{i,j}^{n+1}) - V(\eta_{i,j}^n)}{\Delta t} + \frac{1}{\Delta x} \left[ \sum_{s \in E(i+\frac{1}{2},j)} u_{i+\frac{1}{2},j}^{s,n+1} H_{i+\frac{1}{2},j}^{s,n} - \sum_{s \in E(i-\frac{1}{2},j)} u_{i-\frac{1}{2},j}^{s,n+1} H_{i-\frac{1}{2},j}^{s,n} \right] + \frac{1}{\Delta y} \left[ \sum_{s \in E(i,j+\frac{1}{2})} v_{i,j+\frac{1}{2}}^{s,n+1} H_{i,j+\frac{1}{2}}^{s,n} - \sum_{s \in E(i,j-\frac{1}{2})} v_{i,j-\frac{1}{2}}^{s,n+1} H_{i,j-\frac{1}{2}}^{s,n} \right] = 0 \quad (15)$$

where  $V(\eta_{i,j})$  denotes the volume per unit cell area of the clone considered ( $\eta_{i,j}$  is overloaded for notational simplicity),  $E(i + \frac{1}{2}, j)$ ,  $E(i - \frac{1}{2}, j)$ ,  $E(i, j + \frac{1}{2})$ , and  $E(i, j - \frac{1}{2})$  represent a set of (sub-) clone edges connecting the clone considered to (sub-)clones of neighboring host cells along the east, west, north, and south edge of the clone, respectively. The superscript  $s$  in  $u$  and  $H$  is used simply to denote that they are a quality associated with the clone edges.

The approximate solution  $\eta^{n+1}$ ,  $u^{n+1}$ ,  $v^{n+1}$  can be obtained either by (i) solving the system of nonlinear Eqs. (15), (13), and (14) simultaneously or by (ii) solving a reduced system of equations arising from the substitution of (13), and (14) into (15) Casulli (2009). Such a reduced system of nonlinear algebraic equations in a more compact form is given

by

$$\mathbf{V}(\eta^{n+1}) + \mathbf{T}\eta^{n+1} = \mathbf{b} \quad (16)$$

where  $\eta^{n+1}$  is a vector of the solution at the next time level,  $\mathbf{T}$  is the matrix resulting from the substitution,  $\mathbf{V}$  is the vector of the water volume, and  $\mathbf{b}$  is the known right hand side vector. Note that  $\mathbf{T}$  is symmetric with positive diagonal entries and negative off-diagonal entries. The system of Eq. (16) is (mildly) nonlinear and is solved with the Newton-Raphson method to obtain  $\eta^{n+1}$ . Subsequently, the velocities at the time level  $n + 1$  are computed in a back substitution step from (13) and (14) with the now known  $\eta^{n+1}$ .

Subsequently, the approach described in Section 2.4 is carried out. More precisely, in a scenario of overtopping, the weir formula (1) is used to approximate discharges between sub-clones to update the surface elevations of sub-clones which, in turn, are employed in informing whether sub-clone merging is to be conducted. The resulting surface elevation is subsequently used in updating the set of active cell clones and edge clones prior to the next integration step. The set includes any clone having at least one wet edge and wet clone edge. The wet/dry state of an edge cell is determined based on an edge surface elevation. The edge surface elevation is obtained by taking the mean of the surface elevation of the pair of cells to which it connects (other approaches such as upwinding can also be employed). If the computed surface elevation is greater than maximum pixel depth over the clone edge, this edge is wet. Otherwise it is regarded as dry. It is important to note that the number of cell clones and edge clones can differ from time step to time step due to the possibility of merging and splitting of clones/sub-clones. Further explanation of the numerical implementation is provided in Appendix A.

#### 4. Tests and validation

In this section, the ability of the present algorithm is demonstrated through a set of test cases ranging from idealized test cases to more complex and realistic settings. Boundary conditions are used to drive a flooding cycle in all of the test cases. Atmospheric pressure and wind stress are not considered in the following simulations because those are not expected to play a significant role in any conclusions made. Viscosity  $\mu_t$  is neglected due to relatively coarse gridding. The Manning formula is used to determine a bottom drag coefficient:

$$C_f = \frac{gn^2}{H^{1/3}}, \quad (17)$$

where  $n$  denotes the Manning roughness coefficient. The Manning roughness coefficient and magnitude of gravitational acceleration are set to  $n = 0.02(s/m^{1/3})$  and  $g = 9.81(m/s^2)$  for all simulations. Tests here are divided into three main groups:

1. Channel and block systems.
2. Meandering river and bays.
3. Flow in Buttermilk Bay, a complex bay channel system with measured Lidar bathymetry.

In all numerical tests, the following water surface elevation boundary condition is imposed on the inlet of the computational domain

$$\eta(x, 0, t) = a_0 \tanh\left(\frac{2t}{T_r}\right) \cos(\omega t) \quad (18)$$

where  $a_0$  denotes the forcing amplitude, and  $T_r$  is the ramping time. For the following simulations, the value of tidal frequency is set to  $\omega = 1.4544 \times 10^4 s^{-1}$  and the amplitude of the tide to  $a_0 = 2$  m. For the Buttermilk Bay test case, this amplitude is unrealistically large and is used to demonstrate the robustness of the subgrid model. The tidal-like boundary condition is imposed gradually with a ramp up time of  $T_r = 0.25$  day. Unless otherwise indicated, the maximum and minimum surface elevations used in cloning are set to  $\eta_{Max} = (a_0 + \epsilon)$  and  $\eta_{Min} = -(a_0 + \epsilon)$  with  $\epsilon = 0.2$  m.

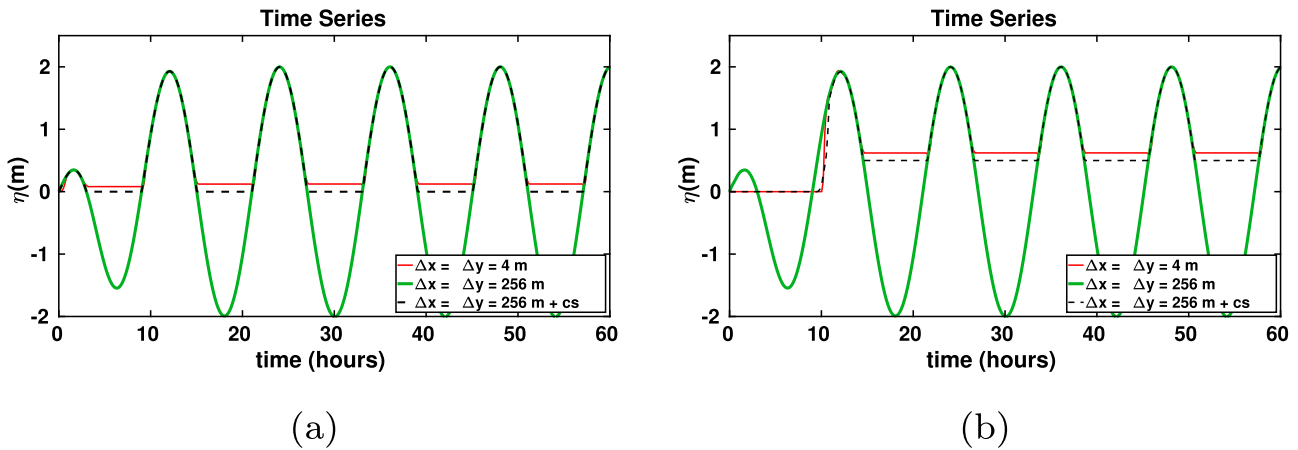


Fig. 13. a) Time series of surface elevation  $\eta$  at a location behind the blockage of 0 m high. b) Time series of surface elevation  $\eta$  at the location behind blockage of 1 m high. Red line is the reference solution (FD/FV). Green line is the level 0 closure subgrid model. Black dashed line is the level 0 closure subgrid model with the sub-clone implementation.

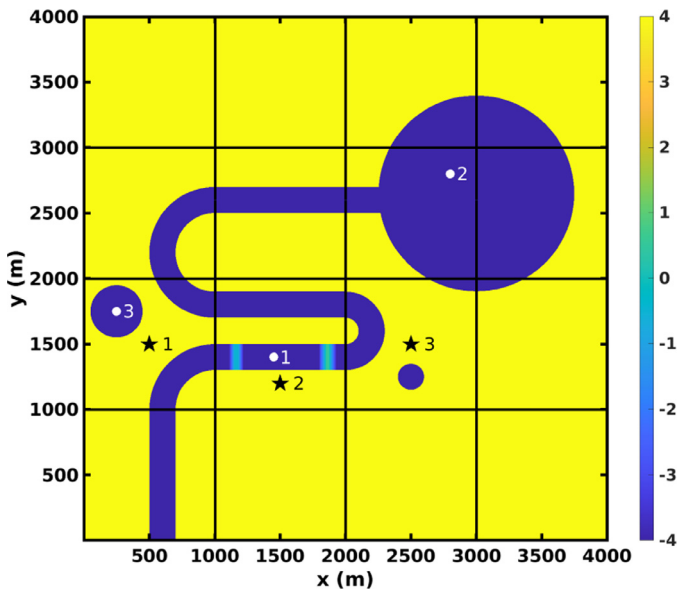


Fig. 14. Meandering River and Bays. Solid black lines depict the computational grid used in coarse grid solutions. Three cells are marked by black stars. Three stations are marked by white circle.

#### 4.1. Channel and block systems

#### 4.2. Permanently disconnected configurations

A first test of the cell and edge clone methodology is performed in an idealized channel with an interior blockage. Two such geometric configurations are depicted in Fig. 8. These systems consist of a channel and a block that splits the channel into two disconnected parts. The surface elevation boundary condition (18) is imposed on the southern part of the computational domain. As a result, the water surface elevation should remain constant for the entire simulation in the secondary channel.

Three simulations with varying grid sizes are performed. The first is a high resolution simulation with  $\Delta x = \Delta y = 2$  m, where this high resolution case is taken as the ground truth reference solution. The coarse grid simulations use  $\Delta x = \Delta y = 256$  m and are run with and without cell and edge clones implementation. Fig. 8 includes grid lines of the coarse grid simulation. It can be observed that, in both configurations, the coarse cell with the block has two wet edges. As the upscaled SWE equations consider subgrid connectivity, an artificial cross flow will be seen in the

secondary channel. To remove this artificial cross flow, the cell with the barrier is cloned twice as there are two groups of connected pixels. This host cell can have two different surface elevations. Cells with blocks and their corresponding cell clones are depicted in Fig. 9.

The time series of water surface elevation in the channel connected to the inlet at station 1 ( $x = 128$  m and  $y = 200$  m) and in the secondary channel, station 2 ( $x = 128$  m and  $y = 1000$  m) of channel configuration A and in the channel connected to the inlet at station 1 ( $x = 128$  m and  $y = 200$  m) and in the secondary channel, 2 ( $x = 600$  m and  $y = 650$  m) of channel configuration B are plotted in Fig. 10 for the three simulations (b and d of this figure plot the surface elevation at the location in front of the barrier). As expected, the high resolution produces a constant water surface elevation in the portion of channel behind the block. However, the time series of water surface elevation of the coarse grid calculation (the green line) is different from the reference solution, where the surface elevation in the range of  $-2$  m to  $2$  m occurs due to an artificial cross flow inside the cell with the barrier. After performing the cell clone procedure for this block cell, the artificial cross flow in the coarse grid is removed and the time series of surface elevation (the black dashed line) is constant.

#### 4.2.1. Inundated configurations

This next test case is similar to the configuration A of channel block system in the previous example, except for the height of the block. In this test, the height of the block enables surface elevation connectivity between two channels as the flow rises above a certain surface elevation (Fig. 11). We use this test case to demonstrate the ability of this algorithm to handle merging and separation of sub-clones. For the first test case, the height of the block is  $b = 0$  m, which is equal to the initial surface elevation of the secondary channel. According to the reference solution when the water surface elevation is less than  $0$  m, the channel splits into two disconnected parts. Thus, the block cell contains two sub-clones at the surface elevation of  $\eta_{Min} < \eta < 0$  and no sub-clones at the surface elevation of  $0 < \eta < \eta_{Max}$ . The block cell is cloned two times based on the connected pixels at the connectivity surface elevation  $\eta = 0$  shown in Fig. 12. Therefore, two parts of the channel are disconnected and there should be no cross flow from the inlet to the second part of the channel. When the water surface elevation reaches  $\eta > 0$  (the first time step), then the original cell with one surface elevation is considered instead of two cell clones. During draining, when water surface elevation reaches zero, the block cell splits into two cell clones with the surface elevation of each clone being that of the block cell.

The time series of water surface elevation at the end of the secondary channel ( $x = 128$  m,  $y = 1050$  m) is shown in Fig. 13a for two different grid sizes ( $\Delta x = \Delta y = 2$  m and  $256$  m). Without clone implementation,

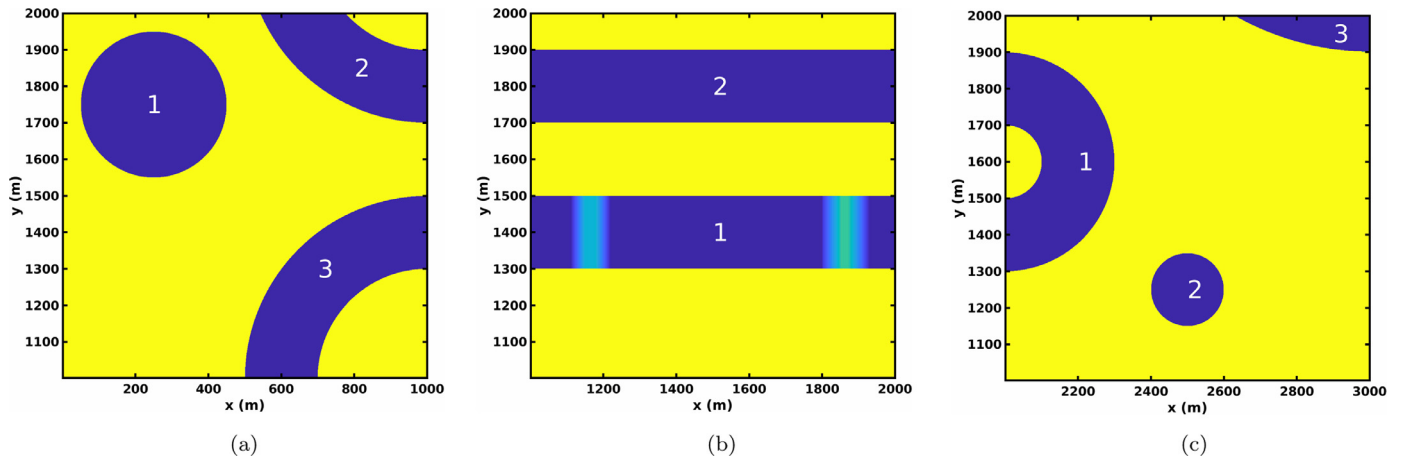


Fig. 15. Cell clones. a) marked cell 1. b) marked cell 2. c) marked cell 3. The number of cell clone is shown on the cells with white numbers.

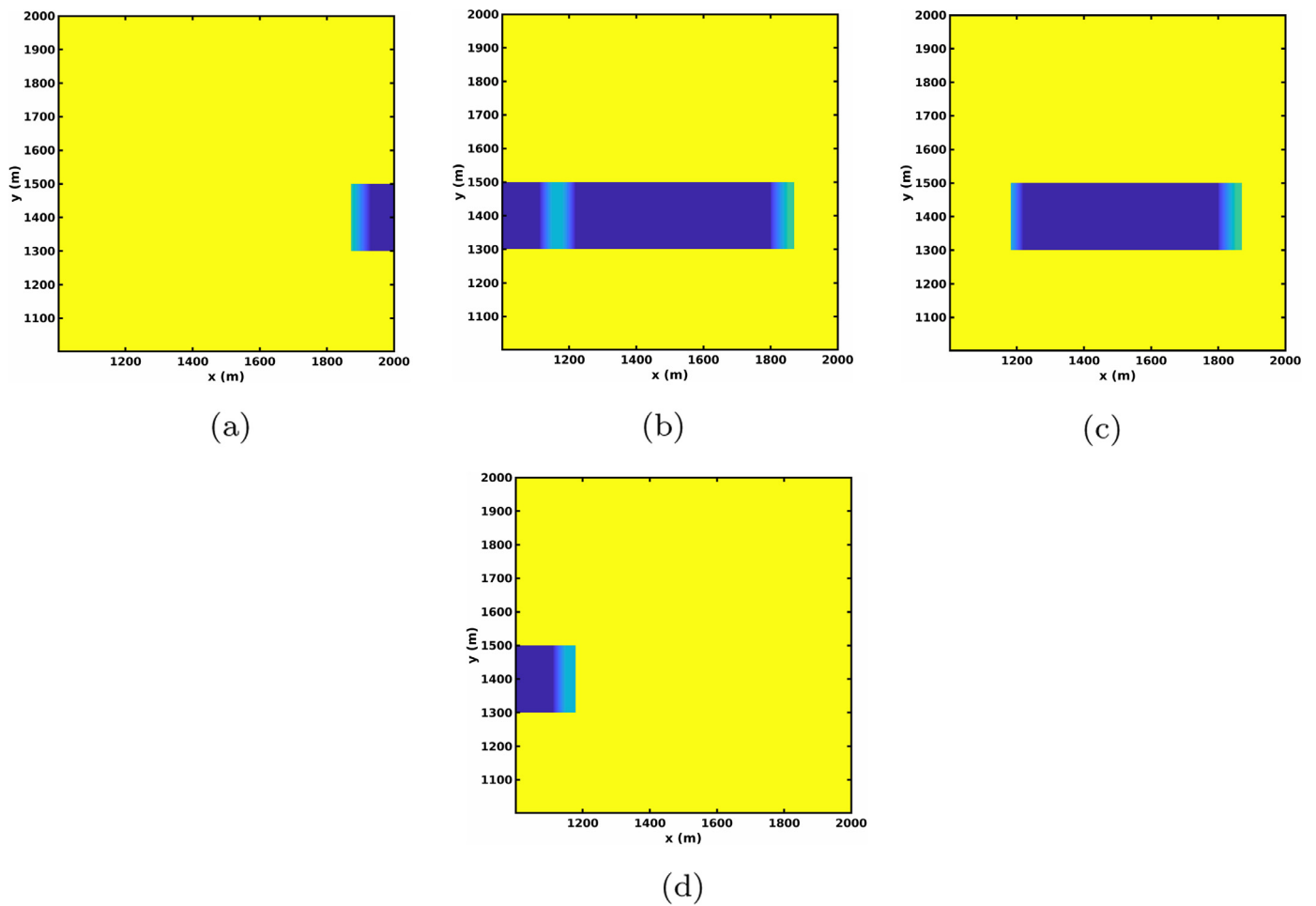


Fig. 16. Sub-clone of marked cell 2. a) sub-clone a at  $\eta = 0.5$ . b) sub-clone b at  $\eta = 0.5$ . c) sub-clone c at  $\eta = -0.5$ . d) sub-clone d at  $\eta = -0.5$ .

the two parts of the channel are connected in the coarse grid calculation resulting in artificial cross flows. With cell clone implementation, the wetting/drying state of the coarse grid solution is similar to the high resolution data.

In a second example, the height of the block is set to 1 m. The initial surface elevation of the secondary channel is set to 0 m. Thus, initially the primary and secondary channels are disconnected and become connected (disconnected) as the surface elevation of primary channel raises above (recedes below) the blockage height. In the coarse grid

calculation with clones, the connectivity surface elevation in the (1,3)<sup>th</sup> host cell is equal to the blockage height; the splitting and merging of sub-clones occurs at this height. Note that when the water surface elevation of the source sub-clone (the clone in front of the blockage) reaches 1 m for the first time, the water surface elevation of the receiving cell is 0 m. This large difference of water surface elevation prevents merging sub-clones because the average water surface elevation of the source and receiver sub-clones will be less than the height of blockage. For the first cycle, the present approach applies the overflow formula to connect

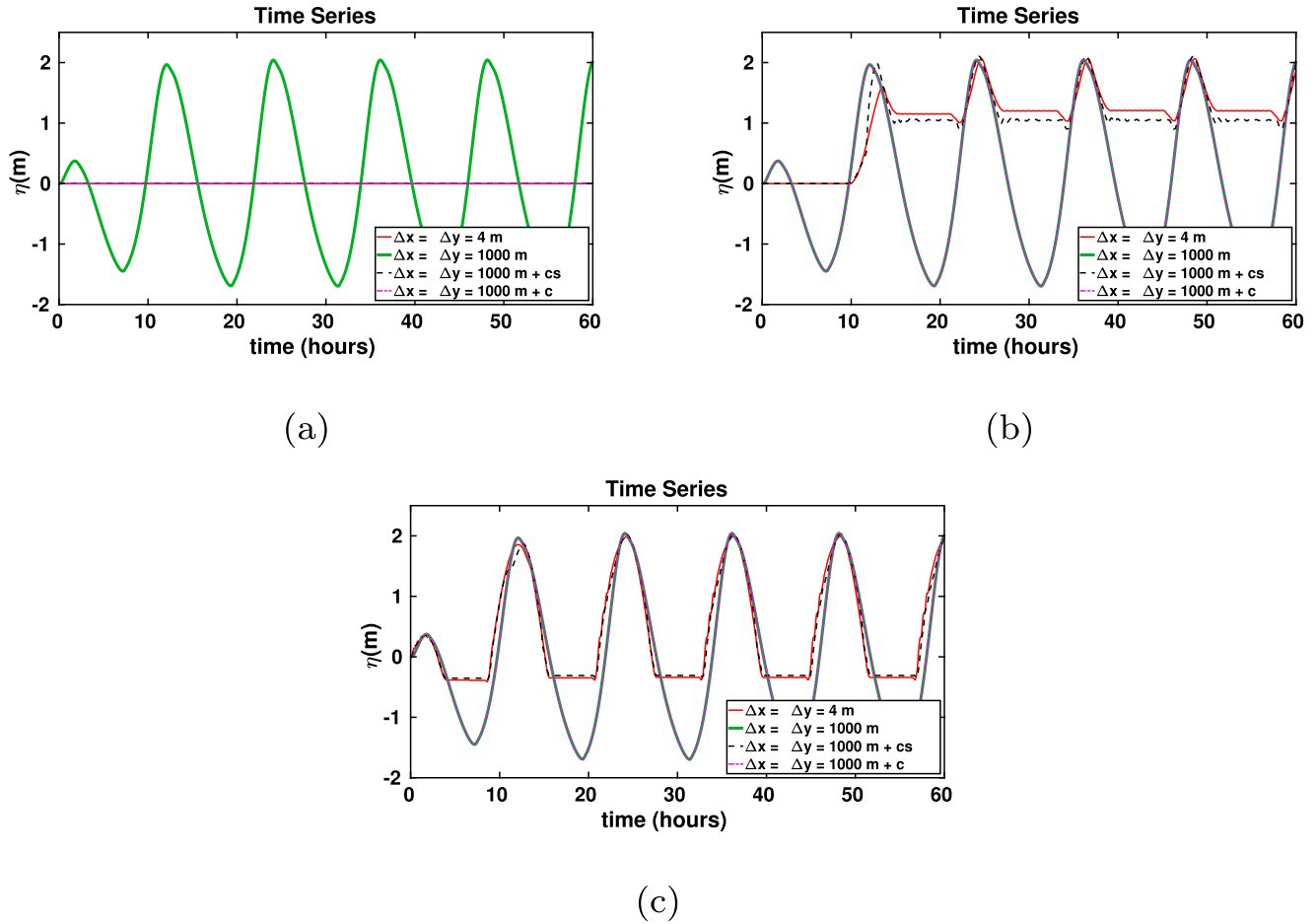


Fig. 17. a) Time series of surface elevation  $\eta$  at location 3. b) Time series of surface elevation  $\eta$  at location 2. b) Time series of surface elevation  $\eta$  at location 1. In the legend, c shows the cell clone implementation and cs shows the sub-clone implementation. ( $\delta x = \delta y = 4m$ ,  $\delta x = \delta y = 1000m$  cell clone implementation and sub-clone implementation are on the top of each other).

the receiver sub-clone to the source sub-clone until the water surface elevation of the receiving clone reaches the height of blockage.

The time series of the surface elevation recorded at the end of channel ( $x = 128$  m,  $y = 1050$  m) are shown in Fig. 13b for the reference solution and the subgrid model without cloning and with the proposed cloning approach. For the high resolution case, it can be seen that the water reaches the secondary channel at an elevation of 1.95 m during the first tidal cycle. Then wetting/drying occurs at the elevation of 1 m as expected. With our proposed technique, the result from the subgrid model with cloning and sub-cloning is in good agreement with the high resolution simulation, while it is not for the subgrid model without clones. It is noted that, in the first cycle, there is a small difference between the high resolution time series of surface elevation and sub-cloning technique. This mismatch in the surface elevation occurs because of the overflow formula.

#### 4.3. Meandering river and bays

An idealized setup reflecting a meandering river with two blocks in the middle as well as three artificial lakes is shown in Fig. 14. The largest lake is connected to the meandering channel. Two narrow barriers can be seen in the middle of the river. The western barrier has an elevation of  $-0.5$  m with eastern barrier elevation  $0.5$  m. A tidal-like boundary condition (see (18)) is imposed on the southern part of the computational domain. The amplitude of the tide is  $a_0 = 2$  m and the tidal period is 12 hours.

Four different simulations are conducted. A high resolution simulation with grid size  $\Delta x = \Delta y = 8$  m is used as the reference solution. Three subgrid simulations on the coarse grid of  $\Delta x = \Delta y = 1000$  m are considered; they consist of (i) subgrid level 0, (ii) subgrid level 0 with Casulli's cell and edge clones (Casulli, 2019), and (iii) our sub-clones approach. As a reminder, the maximum and minimum surface elevations are set to  $\eta_{\text{Max}} = 2.2$  m and  $\eta_{\text{Min}} = -2.2$  m. Fig. 14 shows the coarse grid with three marked cells (black-star symbol). These cells include a disjoint group of pixels at the maximum surface elevation. The cell clones associated with each host cell marked are depicted in Fig. 15. Marked cell 1 and 3 each have three cell clones and marked cell 2 has two cell clones. To find the sub-clone of a cell clone, the number of disjoint connected pixels is checked for each cell clone at a number of surface elevation levels. This process starts at the maximum surface elevation and continues until the minimum surface elevation (with a decremental step of  $\delta\eta = 0.1$  m). For the cell clones of the marked host cells 1 and 3, there is only one group of connected pixels at all levels. Therefore, there are no sub-clones in these cell clones. For the cell clone 1 in the marked host cell 2, the number of disjoint groups of pixels is different as the surface elevations decrease due to the presence of barriers in this cell clone; see Fig. 15 for depiction.

For this simulation, three ranges of water surface elevations are considered in defining clones of the marked host cell 2. When the water surface elevation is  $\eta > 0.5$ , cell clones are used for the system. In the range of  $-0.5 < \eta < 0.5$  sub-clones a and b (see Fig. 16) are considered instead of cell clone 1. For water surface elevations of  $\eta < -0.5$ , sub-

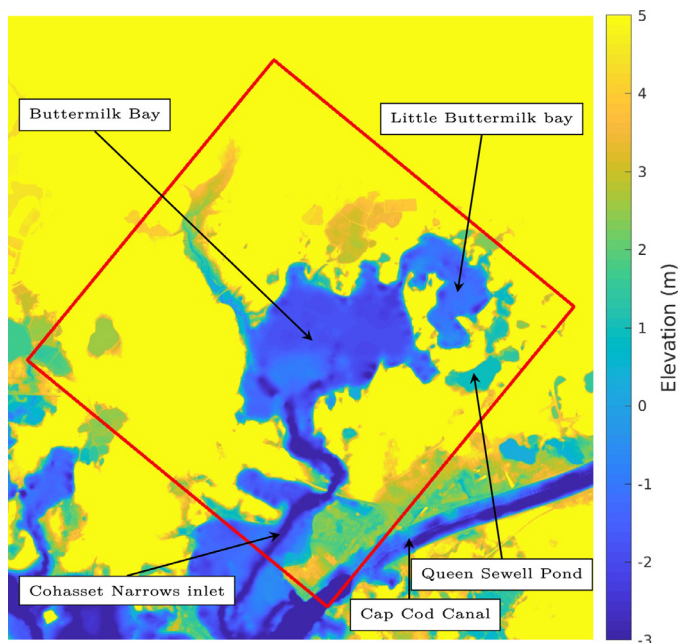


Fig. 18. LiDAR elevation map of Buttermilk Bay area, Massachusetts, USA (41.760N, 70.620W). The red box represents the computational domain Kennedy et al. (2019). (For interpretation of the references to colour in this figure legend, the reader is referred to the web version of this article.)

clones a, c and d represent the cell clone 1. In this simulation, the initial condition is set to 0 m. Thus, for the first cycle of flooding, sub-clone b is connected to sub-clone a through an overflow formula.

Three stations are marked by white circles in Fig. 14. The time series of surface elevation at these locations from all the runs conducted are plotted in Fig. 17a, b and c.

For Station 3 (see Fig. 17), the Level 0 subgrid (line in green) predicts wetting/drying in the small lake, which is not physically correct as

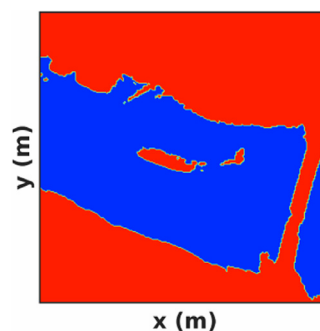
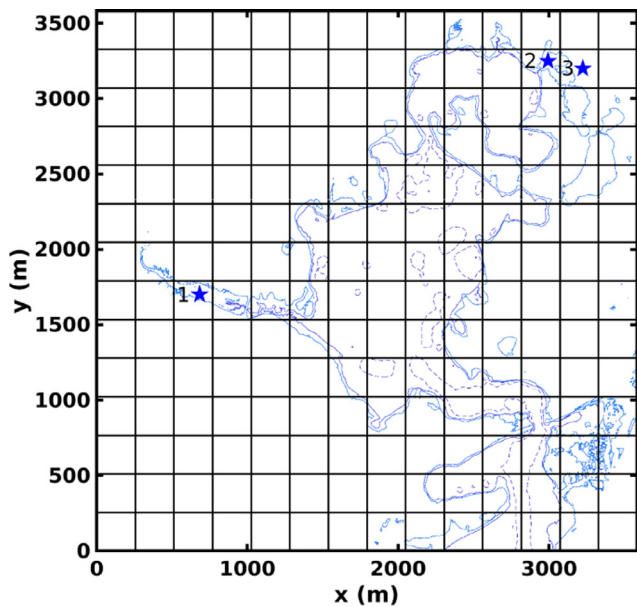


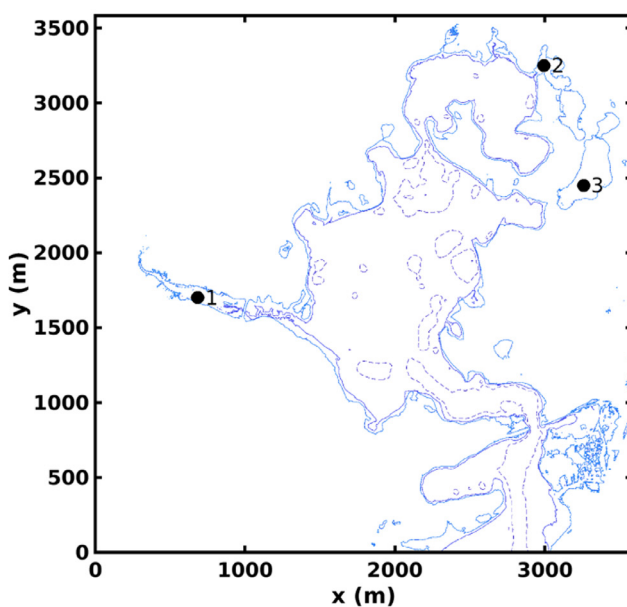
Fig. 20. Wet/dry area for marked cell 1 at the maximum surface elevation. Blue is wet area and red is dry area. (For interpretation of the references to colour in this figure legend, the reader is referred to the web version of this article.)

it is not connected to the inlet. The original cell clone approach and the sub-clone approach proposed yield identical results; both remove this artificial cross flow from the coarse grid calculations. Fig. 17c shows the time series at Station 1, located in the middle of two barriers. The wetting/drying occurs at elevations  $\eta > -0.4$  m for the reference solution. It can be observed that the original cell clone approach behaves identically to the Level 0 solution. The reason is that barriers are determined at the maximum surface elevation in the original cell clone approach. However, the barriers that appear in the lower elevation are part of the continuous path of pixels in the cell clone. Thus, these barrier's effects cannot be captured by the original cell clone approach, and the artificial cross flow still exists in the cell clone's approach. (It is noted that due to the static nature of the original approach, this approach would permanently divide the flow at the maximum surface elevation.) By breaking down the cell clone into sub-clones and connecting and disconnecting the sub-clones, the artificial cross flow can be further removed, thus yielding surface elevations similar to the reference solution.

Fig. 17 b shows the time series at Station 2 situated in the middle of the largest lake. Because the elevation of the barrier is 0.5 m and



(a)



(b)

Fig. 19. a) Solid black lines are the location of coarse grids. Three coarse cells are marked with blue stars. b) Computational domain with three selected contours of bathymetric depth (contour lines: 2 m ; 0 m ; 2 m). (For interpretation of the references to colour in this figure legend, the reader is referred to the web version of this article.)

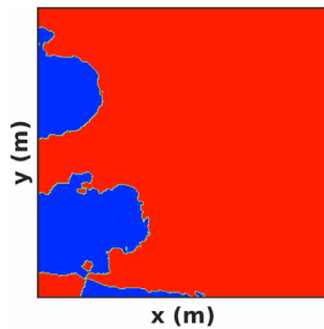


**Fig. 21.** Wet/dry area for marked cell 3. Blue is wet area and red is dry area. (For interpretation of the references to colour in this figure legend, the reader is referred to the web version of this article.)

the initial condition of the water surface elevation is 0 m, the overflow formula is used to connect sub-clone c to sub-clone d (see Fig. 16). Thus wetting/drying happens at the elevation of 0.5 m and sub-clones are merged and split at this elevation. The wetting/drying state with the sub-clone approach is similar to the high resolution run. The coarse grid and static original cell clone runs predict wetting/drying occurs at elevations less than (0.5 m), which is physically incorrect due to an artificial cross flow.

From the results shown above, it can be concluded that the cell clone technique removes the artificial cross flow in the small lakes. However, due to its static nature, the approach cannot accurately capture the effects of two subgrid barriers inside the marked cell 2 as they are submerged at the maximum surface elevation. To capture the effect of these barriers, the sub-clone technique is applied to the computational domain. As a result, marked cell 2 is divided into sub-clones and these sub-clones are merged and split at different surface elevations to capture wetting/drying similar to the high resolution.

#### 4.4. Complex test: Buttermilk bay

In this section, a more realistic computational domain is considered to simulate flooding cycles in Buttermilk Bay, Massachusetts, USA (41.760N, 70.620W) (see Fig. 18). The geometry of Buttermilk Bay includes two narrow channels and two bays, which make it challenging to obtain accurate simulations using traditional techniques and a coarse grid. The computational domain, which has a size of 3854 m  $\times$  3854 m, is shown in the red box in Fig. 18. The driving force for this simulation is a tidal-like elevation boundary (see Eq. (18)), which is imposed along the south part of the red box in Fig. 18.

LIDAR data (in the universal transverse Mercator coordinates) with 1 m resolution is used to describe the bathymetry in all subgrid calculations. The FD/FV subgrid solution based on Casulli's method (Casulli, 2009) with resolution  $\Delta x = \Delta y = 4$  m is used as our reference solution. Kennedy et al. Kennedy et al. (2019) used this test problem to evaluate the performance of the subgrid model with different closures. Therein, they showed the accuracy of the subgrid model for different grid sizes (Kennedy et al., 2019) and also connectivity issues when the computational grids are very coarse.

In this study, we focus on a coarsest grid calculation of  $\Delta x = \Delta y = 256$  m. At this resolution, the subgrid results suffer from the connectivity issues we aim to resolve. Note that we did not consider cell clones and isolated sub-clones with an active area of less than 10% of the coarse grid. The computational grid and three cells with connectivity issues (marked by a blue star symbol) are drawn in Fig. 19a. Fig. 20 shows the wet/dry areas for the marked cell 1 at  $\eta_{Max}$  (red is dry and blue is wet). Two disjoint groups of pixels exist in this cell. The group on the east side of the cell is not connected to the group on the west side due to a barrier which is significantly smaller than the cell. This cell is cloned two times based on a group of connected pixels, to restrict the artificial

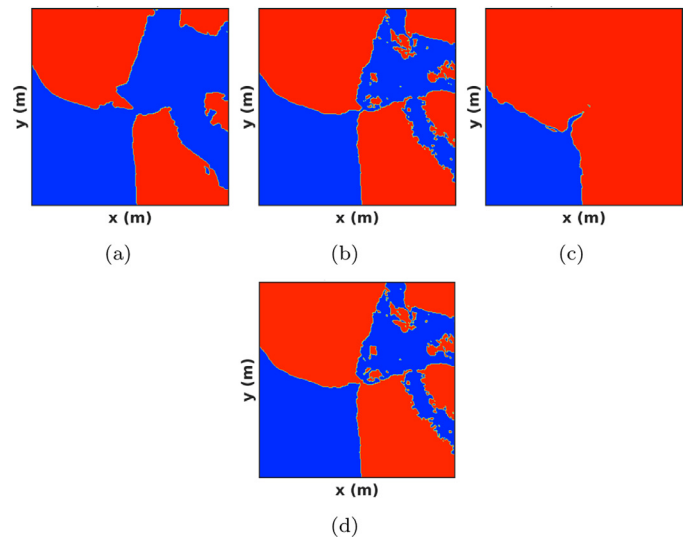


**Fig. 22.** Wet/dry area for marked cell 2. Blue is wet area and red is dry area. a) Wet/dry area at  $\eta = \eta_{Max}$ . b) Wet/dry area at  $\eta = 1$  m. c) Wet/dry area at  $\eta = 0$  m. d) Wet/dry area at  $\eta = 0.98$  m. (For interpretation of the references to colour in this figure legend, the reader is referred to the web version of this article.)

cross flow from the west to the east part of the cell and vice versa (there are no sub-clones for these cell clones).

Fig. 21 shows the wet/dry area at the maximum surface elevation for marked cell 3. A close inspection reveals three disjoint groups of connected pixels. Two of these groups intersect the west edge of the cell and one of them intersects the south edge of the cell. These groups are connected in the subgrid model without cloning. In the clone cell approach, this cell is cloned three times, each of them consisting of a connected path of pixels that restrain the artificial cross flow between these disconnected wet areas (so there is no sub-clone for these cell clones). Fig. 19 shows station 3 located in Queen Sewell pond. This area has a slightly higher elevation than the two main bays and the barrier in marked cell 3 prevents the cross flow to this area.

Fig. 19 shows station 2 located in the area between the Little Buttermilk Bay and Queen Sewell pond that has a relatively higher elevation than the two main bays but lower than Queen Sewell pond. However, it may still be reached by high water elevations.

Marked cell 2 shown in Fig. 19 covers the area between the Little Buttermilk Bay and Queen Sewell pond.

Fig. 22 shows marked cell 2 as well as wet/dry areas at various water level elevations. At the surface elevation of  $\eta_{Max}$ , there is one group of connected pixels at the southwest of the cell and one group of connected pixels at the northeast of the cell, connected by a narrow channel. At the surface elevation of  $\eta = 1$  m, the wet proportion of the channel shrinks and two groups of connected pixels can be discerned. As the surface elevation reduces further to  $\eta = 0$  m, the group of connected pixels in the northeastern part becomes dry. At Fig. 22d, the wet/dry areas are shown at  $\eta = 0.98$  m. This is the point at which the wet areas separate into two disjoint groups. When the surface elevation is  $\eta > 0.98$ , water can connect between the southwest to the northeast and vice versa. Thus,  $\eta = 0.98$  m is a connectivity surface elevation. When the water surface elevation is less than  $\eta = 0.98$  m, this cell (Fig. 22d) splits into two sub-clones. When the water surface elevation of this cell reaches the elevation of  $\eta = 0.98$  m in the first flooding cycle, an overflow formula is used to connect the source sub-clone and the receiver sub-clone. Later, the source sub-clone and the receiver sub-clone merge based on the connectivity surface elevation.

Fig. 23 shows the surface elevation of the wet area for all considered models during the rising tide period ( $t = 0.792, 0.872, 1.000$  day). Fig. 23a-c show the results of the level 0 subgrid solution, level 0 sub-

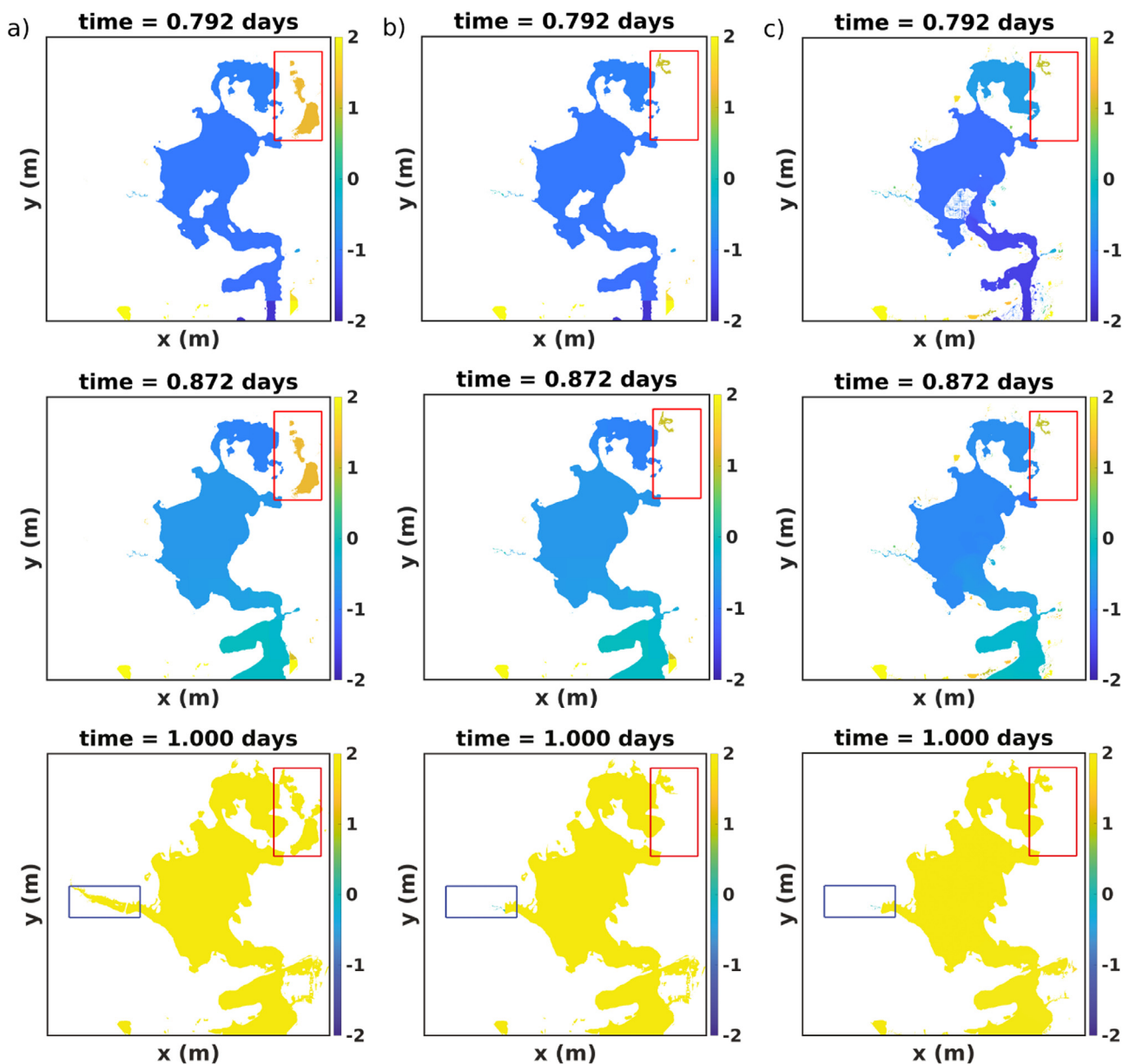


Fig. 23. Water surface elevation solution at various time levels from: (a) Level 0 subgrid model with  $\Delta x = \Delta y = 256m$ ; (b) Level 0 subgrid model  $\Delta x = \Delta y = 256m$  with cell clone and sub-clone; (c) high resolution calculation  $\Delta x = \Delta y = 4m$ .

grid with sub-clones in the computational domain, the reference solution computed on  $4\text{ m} \times 4\text{ m}$  grid, respectively. At  $t = 1$  day, there are additional wet areas in Queen Sewell Pond (see red box in Fig. 23a at  $t = 1$  day) and the west part of main bay (see blue box in Fig. 23a at  $t = 1$  day) in the level 0 subgrid solution in comparison to the reference solution. These additional wet areas result from blocks in the coarse grid are treated as connected areas. This artificial flow can be removed by cloning cell sufficiently to resolve the effect of barriers that are not captured by the subgrid model. It can be clearly observed from Fig. 23b that the subgrid solution with the sub-clone treatment is free of the artificial wet areas seen in Fig. 23a when the subgrid alone is used. The sub-clone subgrid solution indeed is in good agreement with the reference solution. In addition, a small wet area can be seen in Fig. 23c at the time level  $t = 0.792$  and  $0.872$  day (see North west of red boxes). At these time levels, this area cannot be seen in the coarse grid simulation in Fig. 23c. This wet area is captured due to merging sub-clones (marked cell 2) at the surface elevation of  $0.98\text{ m}$  using the overflow formula. By comparing red boxes and blue boxes of Fig. 23b-c at three

time levels, it can be seen that the prediction of surface elevation in the subgrid calculation the cloning technique in the computational domain of the coarse grid matches quite well with the high resolution solution in terms of capturing wetting/drying areas.

In Fig. 24a, the time series of surface elevation is plotted at Station 3 for the reference calculation and subgrid calculations. When the cell clone approach is applied, the time series of surface elevation is identical to the high resolution. Fig. 24b shows the time series of surface elevation at Station 1. Note that this station is in the west part of marked cell 2, i.e. in front of a small barrier (see Fig. 19). Since marked cell 2 splits into two cell clones, the additional water flow is not permitted to go through the barrier. As a result, the effect of the barrier which is smaller than the computational grid can be captured in the subgrid model.

The time series of surface elevation for station 2 is depicted in Fig. 24c. Note that this station is located within marked cell 2 (see Fig. 19). As illustrated in Fig. 22, disconnected groups of wet areas divided by subgrid blocking structured emerge at the height of  $\eta = 0.98\text{ m}$  (see Fig. 22). If water elevation is less than the connectivity surface

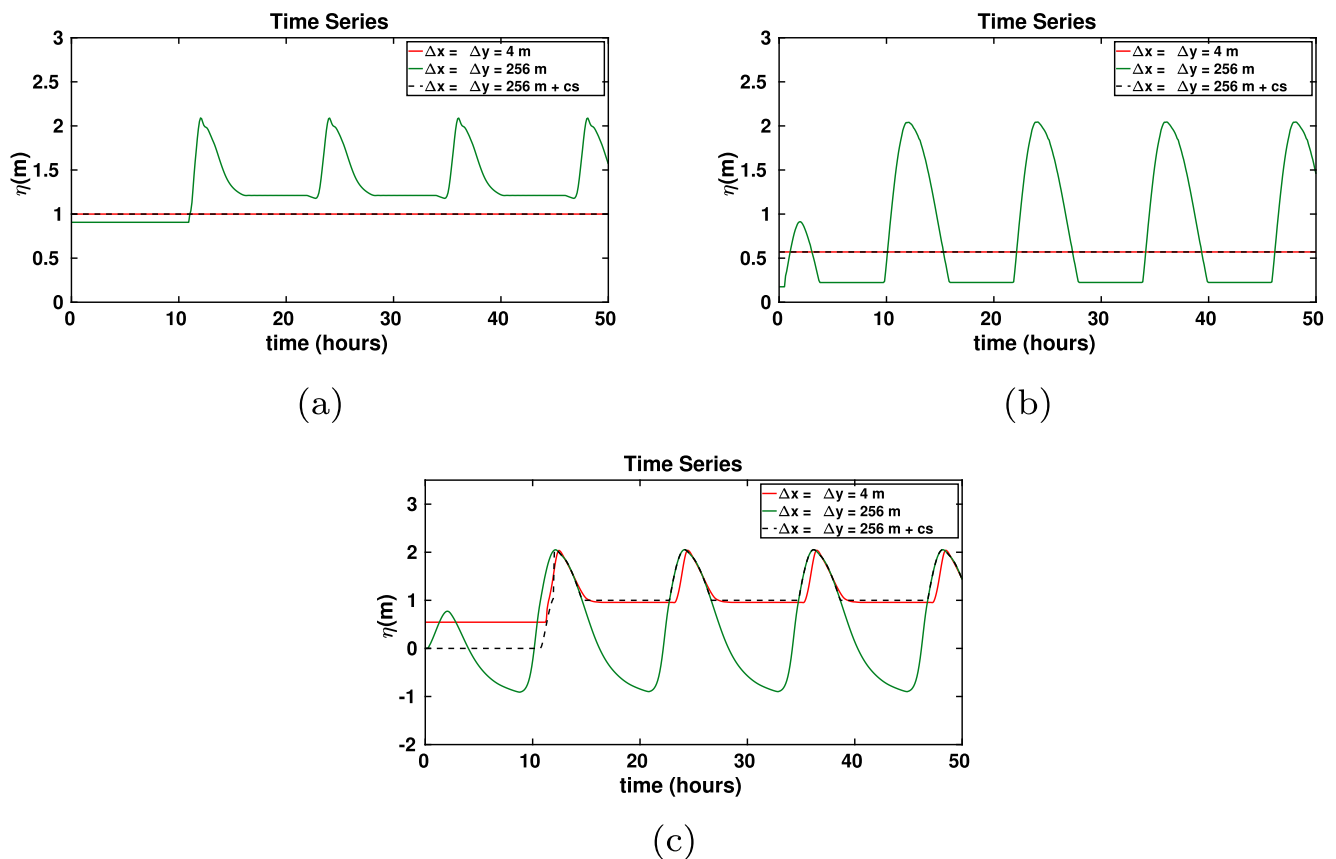


Fig. 24. a) Time series of surface elevation at station 3. b) Time series of surface elevation at station 1. c) Time series of surface elevation at station 2. In the legend, cs shows the sub-clone implementation. Red line is the reference solution (FD/FV). Green line is the level 0 closure subgrid model. Black dashed line is the level 0 closure subgrid model with the sub-clone implementation.

elevation, this cell splits into two sub-clones. When the water surface elevation reaches this height, only one group of connected pixels is considered (see Fig. 22 a). However, there is an exception during the first tidal cycle due to a relatively significant difference of surface elevations between the source clone and the receiver clone, which prevents one cell with a single value of surface elevation. To reduce the large difference, the overflow formula is used to connect the source clone to the receiver clone until the surface elevation of the receiving cell clone reaches the connectivity surface elevation ( $\eta_h = 0.98$  m). Afterward, when the water surface elevation reduces to a value lower than  $\eta_h = 0.98$  m, two sub-clones with two different surface elevations are defined. Otherwise the marked cell with one surface elevation, which is equal to the average surface elevation of receiving clone and host clone is considered. Fig. 24c shows that wetting/drying similar to the reference solution can be captured with a coarse grid solution with the inclusion of cell and edge clones.

## 5. Discussion and conclusions

Using subgrid corrections determined by an averaging process provides increased accuracy in complex shore regions when applying on lower-resolution simulations (Kennedy et al., 2019). However, using an excessively coarse grid can lead to artificial cross-flows between disconnected areas due to barriers that are smaller than the grid size. Although the cell clone approach presented by Casulli (2019) removed the artificial cross flow at the maximum surface elevation, the artificial cross flows may exist at the lower surface elevations as a result of the submerged barriers. In this work, we extend the cell clone approach (Casulli, 2019) by breaking the cell clone down into sub-clones to re-

move cross flow when barriers within the coarse grids are submerged. Splitting and merging sub-clones allows for a more flexible implementation of subgrid models to represent the effect of smaller scale barriers that are submerged and emerged at different water surface elevations. Furthermore, it naturally extends Cartesian grids to restore the high-resolution bathymetric data without sampling or interpolating. This algorithm, in principle is applicable to any flow region with a complex geometry, that may include urban areas and marshland to produce accurate simulations of inundations during flood events.

Our proposed algorithm is implemented in an existing subgrid model (Kennedy et al., 2019) and tested through a variety of tests, ranging from simple channel block systems to a sophisticated natural system, Buttermilk Bay. The model results show that a coarse-grid model, when implementing our approach, has the ability to capture wetting/drying behaviors similar to those obtained from high resolution simulations, without requiring further mesh refinement.

As explained in Section 3.3, we solve a reduced system of nonlinear algebraic equations (Eq. 16) for the surface elevations, which is mildly nonlinear, using the Newton-Raphson method. Solving the system of equations (Eq. 16) requires us to compute the volume and the wet area of coarse cells for each surface elevation. Here, the volume and the wet area of the cells are calculated directly from the high-resolution bathymetric data. For the large grid sizes, these calculations can be very expensive computationally due to the large amount of high resolution bathymetric data inside a coarse grid. To reduce the computational cost, a pre-storage lookup table can be employed to store the volume and the wet area of the cells as a function of surface elevations. Lookup tables can be built once and for all cells as a pre-processing step. Currently, we have not implemented the lookup tables for the cell clone and sub-clone

approach. However, for the subgrid model, we experienced 20% to 30% higher computing time than the standard calculations of the same grid resolutions.

All of the presented test cases were conducted on relatively small Cartesian grids, using a custom-written code. To consider more extreme events, such as hurricane-induced storm surge, much larger grids and parallelization of the algorithm will be required. In principle, the method introduced here can be applied to curvilinear polar, elliptical, and hyperbolic telescoping mesh grids as well as any irregular mesh grids. Future work will focus on incorporating this method into widely-used and available models that have a more significant impact on the field.

### Author Agreement Statement

I the undersigned declare that this manuscript is original, has not been published before and is not currently being considered for publication elsewhere.

I confirm that the manuscript has been read and approved by all named authors and that there are no other persons who satisfied the criteria for authorship but are not listed. I further confirm that the order of authors listed in the manuscript has been approved by all of us.

### Declaration of Competing Interest

Conflict of Interest and Authorship Conformation Form Please check the following as appropriate:

All authors have participated in (a) conception and design, or analysis and interpretation of the data; (b) drafting the article or revising it critically for important intellectual content; and (c) approval of the final version.

This manuscript has not been submitted to, nor is under review at, another journal or other publishing venue.

The authors have no affiliation with any organization with a direct or indirect financial interest in the subject matter discussed in the manuscript

### Acknowledgments

Work here was funded under National Science Foundation, USA grants ICER 1664040 and 1664037, and through a grant from the Joint Airborne Lidar Bathymetry Technical Center of Expertise (JALBTCX), USA. Their support is gratefully acknowledged.

### Appendix A. Numerical implementation

A Fortran-based computer code originally written for an implementation of various forms of subgrid models (and variants of discretization schemes) presented in Kennedy et al. (2019) is modified to handle the clone/sub-clone approach. In terms of its solution algorithm, the two main tasks of the code involve: (i) computing subgrid-related and other necessary quantities, e.g. volume, wet area/fraction, wet cross-section, grid-averaged total water depth, wet/dry status of edges and cells from a given surface elevation solution; and (ii) solving the discretized form of the momentum Eqs. (13)–(14) for the edge-centered  $u$  and  $v$  velocity components and solving the discretized form of the mass Eq. (16) for a solution vector of cell-centered surface elevation  $\eta^{n+1}$ . The former task is accomplished through the use of Fortran objects of derived data type encapsulating data associated with subgrid bathymetry (to be described in brief below) and subroutines/functions computing subgrid-related quantities requested from these objects and a given surface solution vector. For the latter task, we briefly recall below solution procedures in the original code as the clone extends such procedures.

In the original code, for a grid of  $N_x \times N_y$  cells, the latter task uses one-dimensional arrays denoted as

$$\begin{aligned} \mathbf{u}^n &= [u_{i,j}^n]_{i=1,\dots,N_x+1,j=1,\dots,N_y}^T, & \mathbf{v}^n &= [v_{i,j}^n]_{i=1,\dots,N_x,j=1,\dots,N_y+1}^T \\ \boldsymbol{\eta}^n &= [\eta_{i,j}^n]_{i=1,\dots,N_x,j=1,\dots,N_y}^T \end{aligned} \tag{A.1}$$

to store the edge-perpendicular  $u$ -,  $v$ - velocities at the edge-centered vertical and horizontal edges and surface elevation  $\eta$  at the cell center, respectively. Stemming from the use of Fortran, ordering of entries in these 1D arrays is done by mapping an index pair  $\{(i, j)\}$  to a single index in a column major manner. Once the surface elevation  $\eta^{n+1}$  is known, solving the discretized form of the momentum equations is done in a node-by-node fashion; this step is computationally efficient as (13)–(14) are computed only at velocity nodes associated with wet edges, while the value at nodes associated with dry edges is set to zero (i.e. no normal flow is allowed). For the mass equation, the reduced system of nonlinear algebraic Eq. (16) is solved by the Newton-Raphson method, which requires solution of a linear system of equations associated with the Jacobian of the system  $\mathbf{J} = \mathbf{P} + \mathbf{T}$ , where  $\mathbf{P} = \frac{\partial \mathbf{V}(\boldsymbol{\eta})}{\partial \boldsymbol{\eta}}$  is a diagonal matrix whose entries are the values of wet area of cells. Such a linear system is solved by the bi-conjugate gradient stabilized solver (Saad, 1994) where the matrix  $\mathbf{T}$  is stored in an ELLpack-like format mainly for an ease of updating its non-zeros entries especially when the wet-dry pattern changes. Non-zero entries in the row associated with the index pair  $(i, j)$  of the matrix  $\mathbf{T}$  are those associated with the surface elevation of the cell  $(i, j)$  and its wet neighbor cells; for the full grid (no cell clone),  $\mathbf{T}$  has at most five nonzero entries in each row. The dimension of the reduced system of equations is  $N_w \times N_w$ , where  $N_w$  is the number of cells having at least one wet edge; for a problem with wetting/drying,  $N_w$  is time dependent. To keep the code simple, instead of strictly dealing with the  $N_w \times N_w$  system, whose dimension may change with time, we consider an equivalent  $(N_x + 1) \times (N_y + 1)$  system of equations in which the unknown solution vector includes all the cell-centered surface elevation. In this system, an equation associated with a cell having no wet edge (inactive cell) is replaced by  $c\eta_{i,j}^{n+1} = c\eta_{i,j}^n$  (i.e. no change in the value of surface elevation from the previous time step) where  $c$  is a constant used merely to obtain the Jacobin matrix with a properly scaled condition number. Although there is computational expense associated with the inactive cells in this simple approach, such expense is not substantial especially when a coarse grid is considered in a calculation. To accommodate the cell clone and sub-clone approach, which introduce additional DOFs in each host cell and host edge, we use objects that pre-store information of clones and all their sub-clones within the range of  $\eta_{\text{Min}}$  to  $\eta_{\text{Max}}$ . (See Section (2.3 for the procedure to identify sub-clones.) All clones and sub-clones data (in the description below, ‘clones’ refer to both clones and sub-clone) of a host cell are stored in a derived data type with, among several others, the following data fields:

table_type	- table type (raster/lookup table)
nclone	- total number of clones (clones+sub-clones)
tabdat(1:nclone)%b(:, :)	- table of bathymetric data (or lookup table)
tabdat(1:nclone)%b_dim(1:2)	- dimension of table tabdat(i)%b
tabdat(1:nclone)%bmin_max(1:3)	- min, max, avg of bathymetric depth of clones
clone_label(1:nclone, 1:3)	- clone labels (see Section 2.3)
eta_map(1:nclone)	- element indices of clones in a surface elevation
	solution 1D array $\eta$

Note that, in the above description, a%b indicates that b is a member of a derived data a. These data are designed to accommodate two approaches of computing subgrid-related quantities: a direct approach through raster data of a cell (tabdat(i)%b stores portion of DEM pixel in the clone (i), and an approach using lookup tables, which store

the subgrid related quantities at different finite levels of surface elevation in a table before hand for efficiency. In the look-up table approach, the members of `tabdat(1)` store the content of lookup tables; specially, `b_dim(1)` is the number of surface elevation levels, `b_dim(2)` is the number of pre-stored subgrid qualities, `b(1:b_dim(1), j)` stores the  $j^{\text{th}}$  subgrid-related quantity at different levels of surface elevation from `bmin_max(1)` to `bmin_max(2)` with a uniform incremental step of  $(\text{bmin\_max}(2) - \text{bmin\_max}(1))/\text{b\_dim}(1)$ . Note that the direct approach is simple and determines the subgrid quantities exactly for a given surface elevation value; however, it can be computationally expensive with a cost proportional to the number of pixels. The lookup table is very efficient as it requires much fewer operations, i.e. one operation to locate the interval to which the given surface elevation belongs and a few operations for interpolation. This approach requires pre-computing every quantity needed and in general does not yield an exact value (which has a consequence in solving (16)); from our experience, computing the wet surface area  $\mathbf{P} = \frac{\partial V(\eta)}{\partial \eta}$  must be done numerically using a finite difference approximation to achieve convergence in the Newton-Raphson method). Note that `eta_map` storing element indices of clones in the solution vector of surface elevation is used for fetching relevant values to clones of the host cell from a given surface elevation vector.

In solving the discretized form, the solution vectors for the surface elevations are enlarged so that their dimensions are equal to the number of all clones and sub-clones of all  $N_x \times N_y$  host cells. The indexing order in the enlarged one-dimensional array is done in a cell by cell order, i.e. surface elevation solutions of all clones associated with the  $(i, j)^{\text{th}}$  host cell followed by those of the  $(i + 1, j)^{\text{th}}$  host cell. In a short notation,

$$\boldsymbol{\eta}^n = [\tilde{\boldsymbol{\eta}}_{(i,j)}^n]_{i=1,\dots,N_x+1,j=1,\dots,N_y}^T \quad (\text{A.2})$$

where  $\tilde{\boldsymbol{\eta}}_{(i,j)}^n = [\eta^n]_{(r,s,t)}^T$  denotes a surface elevation solution vector of all clones (clones and sub-clones) in the  $(i, j)$  host cell ( $(r, s, t)$  correspond to the clone number, sub-clone level, and sub-clone number as described in Section (2.3). Enlargement of the velocity solution vectors are done in a similar way.

Note that active clones in the computational domain can change due to merging and splitting sub-clones. As done in the full grid case when solving (16), we solve the systems written for all surface elevation DOFs and appropriately modify equations associated with the inactive clones and sub-clones.

The algorithm of computation is summarized as follows:

- 
- 1: **for**  $n = 1$  **to**  $N_t$  **do**
  - 2: For all active clone edges at  $t^n$ : Compute and store the RHS of (13) and (14)
 
$$F_{i+\frac{1}{2},j} \leftarrow \frac{1}{H^n} \left[ H^n_{i+\frac{1}{2},j} u^n_{i+\frac{1}{2},j} - \Delta t F^n_{i+\frac{1}{2},j} \right] \quad G_{i,j+\frac{1}{2}} \leftarrow \frac{1}{H^n} \left[ H^n_{i,j+\frac{1}{2}} v^n_{i,j+\frac{1}{2}} - \Delta t G^n_{i,j+\frac{1}{2}} \right]$$
  - 3: Base on  $F_{i+\frac{1}{2},j}, F_{i-\frac{1}{2},j}, \{H^n_{i,j+\frac{1}{2}}\}, \{H^n_{i,j-\frac{1}{2}}\}$ , set up the sparse matrix  $\mathbf{T}^n$  and the RHS vector  $\mathbf{b}$
  - 4: Solve (16) for  $\boldsymbol{\eta}^{n+1}$  using the Newton Raphson method
  - 5: Update velocities by solving Equation (13) and (14) for  $\{u^{n+1}_{i+\frac{1}{2},j}\}$  and  $\{v^{n+1}_{i,j+\frac{1}{2}}\}$
  - 6: Check the sub-clones surface elevations and apply a weir formula if necessary
  - 7: Update the set of active cell clones based on  $\boldsymbol{\eta}^{n+1}$
  - 8: Update active edge clones based on the new set of active cell clones.
  - 9: **end for**
- 

## References

- Casas, A., Lane, S.N., Yu, D., Benito, G., 2010. A method for parameterising roughness and topographic sub-grid scale effects in hydraulic modelling from lidar data. *Hydrol. Earth Syst. Sci.* 14 (8), 1567.
- Casulli, V., 2009. A high-resolution wetting and drying algorithm for free-surface hydrodynamics. *Int J Numer Methods Fluids* 60 (4), 391–408.
- Casulli, V., 2019. Computational grid, subgrid, and pixels. *Int J Numer Methods Fluids* 90 (3), 140–155.
- Casulli, V., Stelling, G.S., 2011. Semi-implicit subgrid modelling of three-dimensional free-surface flows. *Int J Numer Methods Fluids* 67 (4), 441–449.
- Danielson, J.J., Poppenga, S.K., Tyler, D.J., Palaseanu-Lovejoy, M., Gesch, D.B., 2018. Coastal National Elevation Database. Technical Report. US Geological Survey.
- Defina, A., 2000. Two-dimensional shallow flow equations for partially dry areas. *Water Resour Res* 36 (11), 3251–3264.
- Defina, A., D'alpaos, L., Matticchio, B., 1994. A new set of equations for very shallow water and partially dry areas suitable to 2d numerical models. In: *Modelling of flood propagation over initially dry areas*. ASCE, pp. 72–81.
- Dietrich, J.C., Muhammad, A., Curcic, M., Fathi, A., Dawson, C., Chen, S.S., Luettich Jr, R., 2017. Sensitivity of storm surge predictions to atmospheric forcing during hurricane isaac. *Journal of Waterway, Port, Coastal, and Ocean Engineering* 144 (1), 04017035.
- D'alpaos, L., Defina, A., 2007. Mathematical modeling of tidal hydrodynamics in shallow lagoons: a review of open issues and applications to the venice lagoon. *Computers & Geosciences* 33 (4), 476–496.
- Guinot, V., 2017. Consistency and bicharacteristic analysis of integral porosity shallow water models. explaining model oversensitivity to mesh design. *Adv Water Resour* 107, 43–55.
- Guinot, V., Sanders, B.F., Schubert, J.E., 2017. Dual integral porosity shallow water model for urban flood modelling. *Adv Water Resour* 103, 16–31.
- Hodges, B.R., 2015. Representing hydrodynamically important blocking features in coastal or riverine lidar topography. *Nat. Hazards Earth Syst. Sci.* 15 (5), 1011–1023.
- Hope, M.E., Westerink, J.J., Kennedy, A.B., Kerr, P., Dietrich, J.C., Dawson, C., Bender, C.J., Smith, J., Jensen, R.E., Zijlema, M., et al., 2013. Hindcast and validation of hurricane ike (2008) waves, forerunner, and storm surge. *Journal of Geophysical Research: Oceans* 118 (9), 4424–4460.
- Kennedy, A.B., Wirasaet, D., Begmohammadi, A., Sherman, T., Bolster, D., Dietrich, J., 2019. Subgrid theory for storm surge modeling. *Ocean Modell.* 144, 101491.
- Kerr, P.C., Donahue, A.S., Westerink, J.J., Luettich Jr, R., Zheng, L., Weisberg, R.H., Huang, Y., Wang, H., Teng, Y., Forrest, D., et al., 2013. Us iocos coastal and ocean modeling testbed: inter-model evaluation of tides, waves, and hurricane surge in the gulf of mexico. *Journal of Geophysical Research: Oceans* 118 (10), 5129–5172.
- Kindsvater, C.E., Carter, R.W., 1959. Discharge characteristics of rectangular thin-plate weirs. *Transactions of the American Society of Civil Engineers* 124 (1), 772–801.
- King, I.P., 2001. Modeling of marshes and wetlands. *Journal of Coastal Research* 27, 76–87.
- Li, Z., Hodges, B., 2019. Model instability and channel connectivity for 2d coastal marsh simulations. *Environ. Fluid Mech.* 19 (5), 1309–1338.
- Li, Z., Hodges, B.R., 2019. Modeling subgrid-scale topographic effects on shallow marsh hydrodynamics and salinity transport. *Adv Water Resour* 129, 1–15.
- Luettich, R.A., Westerink, J.J., 2004. Formulation and numerical implementation of the 2D/3D ADCIRC finite element model version 44. XX. Citeseer.
- Platzek, F., Stelling, G., Jankowski, J., Patzwahl, R., Pietrzak, J., 2016. An efficient semi-implicit subgrid method for free-surface flows on hierarchical grids. *Int J Numer Methods Fluids* 80 (12), 715–741.
- Roig, L.C., 1989. A finite element technique for simulating flows in tidal flats. University of California, Davis.
- Saad, Y., 1994. Sparskit: a basic tool kit for sparse matrix computations.
- Sanders, B.F., Schubert, J.E., Gallegos, H.A., 2008. Integral formulation of shallow-water equations with anisotropic porosity for urban flood modeling. *J Hydrol (Amst)* 362 (1–2), 19–38.
- Sehill, A., Lang, G., Lippert, C., 2014. High-resolution subgrid models: background, grid generation, and implementation. *Ocean Dyn* 64 (4), 519–535.
- Stelling, G.S., 2012. Quadtree flood simulations with sub-grid digital elevation models. In: *Proceedings of the Institution of Civil Engineers-Water Management*, 165. Thomas Telford Ltd, pp. 567–580.
- Viero, D.P., Valipour, M., 2017. Modeling anisotropy in free-surface overland and shallow inundation flows. *Adv Water Resour* 104, 1–14.
- Volp, N., Van Prooijen, B., Stelling, G., 2013. A finite volume approach for shallow water flow accounting for high-resolution bathymetry and roughness data. *Water Resour Res* 49 (7), 4126–4135.
- Wang, H.V., Loftis, J.D., Liu, Z., Forrest, D., Zhang, J., 2014. The storm surge and sub-grid inundation modeling in new york city during hurricane sandy. *J Mar Sci Eng* 2 (1), 226–246.
- Whitaker, S., 2013. *The method of volume averaging*. 13. Springer Science & Business Media.
- Wu, G., Shi, F., Kirby, J.T., Mieras, R., Liang, B., Li, H., Shi, J., 2016. A pre-storage, subgrid model for simulating flooding and draining processes in salt marshes. *Coastal Eng.* 108, 65–78.
- Zachry, B.C., Booth, W.J., Rhome, J.R., Sharon, T.M., 2015. A national view of storm surge risk and inundation. *Weather Clim. Soc.* 7 (2), 109–117.